Final Project Report: Department of Energy, Nuclear Energy University Programs (DOE-NEUP)

Award Number: DE-NE0008703

Project Title: CFA-17-12798: Nanostructured Ceramic Membranes for Enhanced Tritium Management

Technical Work Scope Identifier No: FC-1.3b Fuel Processing Off-Gas Management- Tritium Separations Technology

Lead Institution

Clemson University

Sikes Hall

Clemson, SC 29634

Principal Investigator:

Dr. Kyle S. Brinkman

Professor

Materials Science and Engineering,
Clemson University

161 Sirrine Hall; Clemson, SC 29634

ksbrink@clemson.edu

Co-Principal Investigators (Investigator, *Department,* University)

Jianhua (Joshua) Tong, *Materials Science and Engineering,* Clemson

Jake Amoroso, *Environmental and Chemical Process Technology,* Savannah River National Laboratory

CONTENTS

Project Title: CFA-17-12798: Nanostructured Ceramic Membranes for Enhanced Tritium Management 1

Technical Work Scope Identifier No: FC-1.3b Fuel Processing Off-Gas Management- Tritium Separations Technology 1

1. Excusive summary 3

2. Project Objects 4

3. Background 5

3.1 Simple oxides 6

3.2 Doped perovskite zirconates 6

4. Approaches and Results 7

4.1 Methods 7

4.1.1 Powder synthesis 7

4.1.2 Nanostructured membrane fabrication 7

4.1.3 MATERIALS characterization 9

4.2 Results and key findings 10

4.2.1 Simple oxides: cold sintering of TiO_2 10

4.2.2 Simple oxides: traditional sintering of TiO_2 12

4.2.3 Insights into the proton transport mechanism in TiO_2 simple oxides by in-situ Raman spectroscopy 15

4.2.4 Perovskite oxide materials: Cold sintering of BZY20 20

4.2.5 Initial study on catalyst addition strategies 27

4.2.6 Process level characterization parameters: surface exchange and diffusion coefficients 29

4.2.7 Transport Model and Process Based Economic Analysis 35

Conclusions 42

NEUP Publication and Presentation List 43

References 43

1. EXCUSIVE SUMMARY

This project focuses on the novel use of interfacial hydrated layers in ionic conducting ceramic materials for tritiated water (HTO) adsorption and recovery. Low-temperature water adsorption properties of nanoscale structured ceramics combined with hydrogen isotope exchange in their hydrated layers could provide a low-cost and transformative avenue to address tritium management challenges.

In this project, two categories of materials were explored including i) simple oxides (TiO_2), ii) perovskite phases based on zirconates ($BaZr_{0.8}Y_{0.2}O_{3-\delta}$ (BZY20), $BaCe_{0.7}Zr_{0.1}Y_{0.1}Yb_{0.1}O_{3-\delta}$ (BCZYYb)). Nanostructured ceramic membranes were fabricated from the crystalline materials utilizing three principal methods: i) conventional sintering, ii) two step sintering, iii) spark plasma sintering (SPS), and iv) cold sintering.

Nanostructured TiO_2 membrane was fabricated through traditional sintering method to investigate the absorption, mobility, and isotope exchange effect. The increased conductivity of nanostructured TiO_2 membrane in the wet atmosphere and its polarization behavior confirm the existence of the proton conductivity in the nanoscale TiO_2 membrane at low temperatures (< 250 ºC). The difference of proton conductivity in H_2O and D_2O reveals the hopping mechanism of the proton conduction. In addition, the thermo-gravimetric analysis reveals strong water uptake below 250 ºC explains the high proton conductivity at low temperatures. A high proton conductivity was achieved in the nanostructured TiO_2 membrane in wet atmosphere. Further study about the relations among the grain size, porosity, hydration/dehydration behavior, and proton conductivity reveal the difference of proton conductivity was probably caused by the "free water" in the membranes. The smallest grain size shows the strongest water uptake and de-absorption ability, which related to the highest proton conductivity. Control of interfacial proton conductivity was demonstrated by changing the grain size and porosity of the nanostructured membrane. Furthermore, in-situ Raman was used to perform the isotope exchange experiment to identify the OH and OD vibrating bonds at room temperature. There is no bonding change from OH to OD at room temperature, indicating there is no isotope exchange. The protons are transported as hydroxide ions, hydroxonium ions, or higher hydrated protons, the protons use the water molecule as a vehicle.

A cold sintering pretreatment of BZY20 helped to produce dense ceramics at a moderate temperature of 1500ºC (200ºC lower than the traditional sintering temperature). The as-fabricated BZY20 pellets showed a phase-pure perovskite structure, high relative density, and desired microstructure. A further comparative study with the control BZY20 pellets indicated introducing the proper amount of $BaCO_3$ on the precursor particle surface and the high green density for the green pellets with homogenous microstructure achieved by cold sintering pretreatment were responsible for lowering the final sintering temperature. Furthermore, the as-fabricated BZY20 pellets showed comparably high proton conductivity to conventionally processed state-of-the-art BZY20 pellets. Effects of sintering process and water amount on the morphology of BZY20 were investigated. It was concluded that more uniform grain sizes, as well as lower density, were obtained by decreasing sintering temperature. Regarding the water amount, higher water concentration results in larger grain size and higher relative density. The optimized cold sintering conditions, including tailored porosity could provide options for nano-structure membranes of use in this project. Pellets of the BCZYYb materials were also fabricated directly using the simple and cost-effective solid state reactive sintering (SSRS) method from raw precursors of respective oxides and carbonates. EIS results demonstrated the isotope effect which is more significant at low temperature.

The fundamental materials properties were also obtained and further used in the modeling effort and documents completion of process level characterization. These studies include adsorption capacity of nanostructured TiO_2, BZY20 and BCZYYb (with and without catalysts) as function of grain size and porosity, the evaluation of different techniques such as Electrical Conductivity Relaxation (ECR) and in-situ Raman studies to obtain surface exchange coefficient k and diffusion coefficient D as a function of temperature. This data was provided to SRNL partners for use in modeling effort and process level economic analysis. At lower temperature (<300 °C), $\boldsymbol{k}$ and $\boldsymbol{D}$ can be determined by Raman and conductivity measurements (through Nernst-Einstein equation). At higher temperature (>300 °C), Electrical Conductivity Relaxation (ECR) fitting was used to extract $\boldsymbol{k}$ and $\boldsymbol{D}$.

Effect of catalyst on the proton conduction was also investigated. NiO, Fe_2O_3 and CuO were mixed with nano scale TiO_2 powder, respectively, followed by densification with SPS method at 700 °C. Improved conductivity was observed for the sample with catalyst at low temperatures. At room temperature, the proton conductivity increased by a factor of 5.5, 1.7 and 2.9 with NiO, Fe_2O_3 and CuO as catalyst, respectively. Using an optimum amount 5 mol% Cu as catalyst, a BZY20 pellet with an average grain size around 120 nm and relative density of 97% was obtained. Additions of Cu in favor of densification with limited coarsening as compared to Ni. A comparison of cold sintering with two-step sintering indicates the former is better at obtaining a dense pellet with smaller grain size, A significant hydrogen isotope effect was found in porous nanostructured TiO_2 at 100 ° C as evidenced by in-situ Raman studies.

Modeling effort and process level economic analysis was conducted by SRNL partners. We rely on extrapolation of data from H/D systems, and associated separation factors to understand the process of tritium absorption and recovery in an isotope exchange bed. This milestone focuses on process-based economic analysis which considered membrane materials, process equipment, and energy cost as a function of process conditions. Ultimately, this preliminary evaluation estimates a system based on an adsorption/regeneration cycle utilizing a 1.26 m3 bed would have annual operating costs about $33K to selectively remove tritium from 175 tonnes of low-tritiated water. In this configuration, the cost of detritation is approximately $0.19/L.

2. PROJECT OBJECTS

The overall project objectives were to systematically fabricate and characterize the nanostructured proton conducting oxides followed by bench-scale membrane separations testing and process-level economic analysis. Two primary objects are A) fundamental understanding of water adsorption and isotope exchange as a function of interfacial structure and chemistry, B) data collection and preliminary process design including cost/benefit analysis and a technology maturation plan for ceramic membrane treatment of high-volume aqueous streams with low tritium concentration.

Task A focused on materials selection, processing, and structural characterization. Characterization of hydrogen isotope adsorption, mobility, and isotope exchange. This will be correlated with the physical microstructures of the ceramics produced by the various preparation and consolidation methods outlined in Task 1 to establish the influence of average grain size, density of grain boundaries and porosity on the isotopic exchange characteristics. The kinetics of isotope exchange H/D will be explored by time

dependent EIS measurements and compared with results from vibrational spectroscopy. Materials selection was performed including identifying the best candidate materials for further adsorption membrane experiments.

Task B focused on computational predictions and economic analysis. The separation properties such as permeation fluxes for H_2O and D_2O and separation factors of D_2O and HDO from H_2O for the oxide materials will be measured by using packed bed/membrane testing by online mass spectroscopy to monitor the in-situ compositions of the influent and effluent. The influence of operation temperature, pressure difference on the concentrations of each species will be determined. The effect of the grain size, surface area, and porosity will also be studied.

Overall, the work is geared towards understanding fundamental adsorption/exchange mechanisms and structural/chemical properties of the nanostructured membranes can be used to influence waste form design as well as separations processes of interest to DOE.

3. BACKGROUND

Tritium (T), is a radioactive isotope of hydrogen with a half-life ($t_{1/2}$) of ~12.3 years, is chemically identical to hydrogen, and can undergo isotope exchange to form tritiated water (HTO). Tritium can undergo isotope exchange reactions with protium (^1H) and D containing molecules (e.g., H_2O, H_2, CH_4, etc.) during nuclear processing and become incorporated into the molecular structure of these chemicals found in in plant products and waste streams. Although T is not a strong beta emitter, it is a radiation hazards when inhaled, ingested via food or water, or absorbed through the skin. Due to the potential health hazard from the ingestion or adsorption of T, emissions to the environment are regulated by the U.S. Nuclear Regulatory Commission and the U.S. Environmental Protection Agency), and, in the UK, by the Environment Agency. The T present in used nuclear fuel may be handled in reprocessing scenarios by either: i) a pre-treatment step before fuel dissolution which concentrates tritium in a low-volume gas stream, or ii) direct dissolution of used fuel resulting in a high-volume aqueous stream with low tritium concentrations (*1 x 10^{-5} or 10's ppm)*[1]. The technology pioneered in this proposal addresses the latter strategy of tritium management in high volume aqueous waste streams where the current baseline technology is the Combined Electrolysis Catalytic Exchange (CECE) process used by Atomic Energy of Canada Limited at the Chalk River Plant in Canada[2]. More recent approaches to address this challenge have focused on zeolite-based absorbents operating as pervaporation membranes and graphene-based membranes for tritiated water separation[3].

Recently, there has been increased attention on ionic conducting ceramics as enabling technologies in the nuclear industry including, their use as proton conducting ceramics for tritium sequestration[4], electrolysis[5], and separations[6]. Proton ceramic electrolysis cells have been investigated as a method of processing HTO in the International Thermonuclear Experimental Reactor fusion reactor system. Prior work has demonstrated significant advantages of ceramics due to the enhanced radiation stability and the ability to perform electrolysis at elevated temperatures in the vapor phase, which avoids the potential exposure and associated risk of liquid HTO. Most of the known ceramic proton conductors such as $(Ba,Sr)CeO_3$ and $BaZr_{0.8}Y_{0.2}O_{2.9}$ rely on proton transport within the crystalline lattice[7]. However, a number of recent studies have reported proton conductivity at low-temperature in zirconia[8], ceria[9],

and titania[10] based systems. This proton conductivity has been attributed to absorbed water at the grain boundary interfaces in these systems. This effect vanishes at temperatures greater than 500°C, where dehydration of the interfaces occurs, and the conductivity reverts to that of the bulk material. There is a demonstrated grain-size effect with the enhanced disorder and elevated surface energy at nanoscale grains making dissociated water adsorption more favorable. The interfacial hydrated layer may consist of hydroxyl species bound to the ceramic surface and surface hydroxyl layers with varying degree of bonding strength. Recent work on isotope exchange reactions in zirconia systems monitored by thermogravimetric analysis and spectroscopic gas phase analysis as a function of time and temperature revealed that the strongly bound surface hydroxyl groups (OH) exhibited full H/D exchange (OD) at 400°C within 120 minutes, and at temperatures near 50°C, weakly bound free water molecules at the interface completed H/D isotope exchange within 10 minutes[8].

3.1 SIMPLE OXIDES

A specific class of materials typically referred to as proton conducting ceramics (PCCs) exhibits proton conductivity at much higher levels than the conventional oxygen ion conducting oxides (e.g., yttria-stabilized zirconia, YSZ) at intermediate-temperature (IT) temperatures (400-800°C). Except for the bulk IT proton conduction, the interfacial proton conductivity has been observed at low-temperature (LT) regime (<400°C) for some simple oxide systems such as zirconia, ceria, and titania which usually do not exhibit bulk proton conduction. The origin of the proton conductivity in these systems has been attributed to absorbed water at the grain boundaries, which reverts to that of the bulk material because the dehydration of the interfaces occurs at temperatures higher than 500°C. For example, Wang *et al*.[11] modified the grain boundary of samarium doped ceria (SDC) with sintering aids such as sodium carbonate resulting in nano-composite with enhanced proton conductivity in the temperature range from 200-600°C.

3.2 DOPED PEROVSKITE ZIRCONATES

In addition, there has been recent interest in PCCs as enabling technologies in the nuclear industry including, their use as LT proton conducting ceramics for tritium sequestration, electrolysis, and separations. In recent years some promising advances have been made on LT-PCCs based on doped perovskite oxides. Pergolesi *et al*[12] demonstrated that conventional perovskite oxide $BaZr_{0.8}Y_{0.2}O_{3-\delta}$ (BZY20) retained elevated levels of proton conductivity at temperatures as low as 350°C when processed as epitaxial thin films. This is an extension of commonly accepted physical behavior observed in the IT range where the bulk conductivity contributes more than the grain boundaries to ionic conduction because of the removal of grain boundary in the epitaxial films. However, as pointed out by Malavasi *et al*[13] nanoscale materials exhibit significant nanoionic effects due to short diffusion lengths and a high density of interfaces resulting in effective properties of the material dominated by the grain interfaces[14]. In the IT range, the increased grain boundary area encountered in nanomaterials typically behaves as a "blocking" layer for ionic transport. However, recent work has provided evidence for tailoring the behavior of proton transport at the grain interface by introducing catalytic nanoparticles, especially in the LT regime. Clark *et al*.[15] have observed that Ni nanoparticles and nanofilms in $BaCe_{0.7}Zr_{0.1}Y_{0.1}Yb_{0.1}O_{3-\delta}$ (BCZYYb) grain boundary could enhance the LT proton conductivity.

4. APPROACHES AND RESULTS

4.1 METHODS

4.1.1 POWDER SYNTHESIS

Solid state reaction synthesis is the most widely used method for the preparation of polycrystalline solid powders from a mixture of solid-state precursor materials. Solids do not react together at room temperature over normal time scales and it is necessary to heat them to high temperatures. The factors on which the feasibility and rate of a solid-state reaction depend include, reaction conditions (e.g., temperature, time, and atmosphere), structural properties of the reactants, surface area of the solids, their reactivity and the thermodynamic free energy change associated with the reaction. The reactants selected to prepare a solid crystalline compound were metal oxides or carbonates. As the increase in surface area can enhance the solid-state reaction rate, fine-grained materials should be used if possible. To improve composition accuracy, the reactants were usually dried thoroughly prior to weighing. The heating program was selected based on the form and reactivity of the reactants.

Wet chemistry synthesis allows the attainment of multicomponent metal oxides with controlled size and shape, high chemicophysical reactivity and very high purity control. Such control on the produced materials, requires the development of synthesis starting from precursors in the form of metal salts solutions. The processes are based on the hydrolysis or on the reduction, in water or in organic solvents, or metal precursors, caused by pH changes or by the addition of reducing agents. The optimization of the produced systems is performed throughout an accurate tuning of all synthesis parameters. Solution processing method is based on citric-EDTA acid complexing sol-gel method, which be a modified Pechini method.

Solid state reactive sintering (SSRS) is developed for one-step sintering to synthesis high quality, fully dense and relative low sintering temperature pellets with the help of sintering aids (e.g., NiO, CuO and ZnO). Similar with solid state reaction, SSRS method also start with simple metal oxides or carbonates. By well mixing with ball milling in proper dispersant, dry fine powders could be achieved with string on a hot plate. Subsequently, green pellets were pressed with die and table press. Finally, the dense sintered pellets were obtained with a specific heating program which different by samples in a simple and cost-effective way.

Modified Pechini Method based on the Pechini Method which was widely used in nanocrystal synthesis. By controlling the ratio of ethylene diamine tetraacetic acid (EDTA), citric acid and ammonium hydroxide, nitrates or acetates for each element could be dissolved and homogenously formed polymer-oxide composite, in stoichiometry ratio of the final material. Following with calcination, combustion and firing in proper temperature, nanoscale powders can be obtained.

4.1.2 NANOSTRUCTURED MEMBRANE FABRICATION

It is widely known that microstructure of the ceramics has significant impact on the performances. Certain crystalline powder solids could gain full density and translucency by solid-state sintering was an important milestone for modern technical ceramics. But these final-stage sintering processed are always accompanied by rapid grain growth.[16][17] These has greatly hampered efforts to produce ceramic

membranes with nanometer-scale structure. A number of new methods have been developed to facilitate the cost-effective preparation of nanostructured membranes for practical applications.

(a) Conventional sintering

The conventional sintering process usually consists of heating a performed powder (raw or blended materials) at high temperatures, although slightly lower than the melting point, during minutes to hours. The sintering of the materials is driven by the decrease of specific free surface area. What's more, the excess surface energy is a necessary but not a sufficient condition for sintering. Diffusion promoted by thermal energy and local driving forces are also necessary conditions.[18]

(b) Two step sintering

Two step sintering uses two different sintering temperatures. The first sintering temperature should guarantee a relative density higher than 75% of theoretical sample density. The sample were then cooled down and held at the second sintering temperature until densification is completed. As a promising alternative method to prepare fine microstructure dense ceramics, the two-step sintering method has been proved to be less costly and more efficient[19], which has been used to solve the issue of the narrow processing window of the sintering temperature in lead-based or lead-free ceramics, including $BaTiO_3$[20],[21], $Bi_{0.5}Na_{0.5}TiO_3$.[22],[23] In addition, the two-step sintering can also reduce both the pores of the ceramics and the volatilization of the substances with a low melting point, which is helpful in preparing the (K, Na)NbO_3-based ceramics.[24],[25] Wang et.al successfully prepared densified BZY samples by a two-step reactive aid sintering (TRAS) method with 1 wt.% B_2O_3-Li_2O sintering acid.[26] Chen et.al prepared fully dense cubic Y_2O_3 with a grain size of 60 nm via a simple two-step sintering method, at temperature of about 1000 °C without applied pressure. However, the grain size changes in tetragonal zirconia and hexagonal alumina were not statistically significant.

(c) Solid-state reactive sintering

The recently developed solid-state reactive sintering (SSRS) method significantly simplifies the fabrication process for proton conducting ceramics by combining phase formation, densification and grain growth into a single high-temperature sintering step. In the SSRS method, the use of a small amount of a properly chosen sintering additive enables the direct solid-state reaction, densification and grain growth of inexpensive precursor oxide/carbonate powders to produce the desired phase-pure ceramic component in a single high-temperature step. In addition to lowering the sintering temperature by 200-400 ºC compared to conventional sol-gel processes. The SSRS mechanism is clarified through a systematic study of the effect of metal oxide sintering additives on the densification of proton conducting ceramics $BaZr_{0.8}Y_{0.2}O_{3-\delta}$ (BZY20).[27]

(d) Spark plasma sintering

Spark plasma sintering (SPS) is a new technique which takes only a few minutes to complete a sintering process compared to conventional sintering. High DC pulse is passed the sample between graphite electrodes and axial pressure is simultaneously applied from the beginning of the sintering cycle. The sample is heated by the Joule-heating and the sparking among the particles of sintered materials leads to the faster heat and transfer instantaneously. This high sintering rate is possible in SPS sintering since high heating rate can be easily attained which may exceeding 300 °/min, hence a temperature of 1200 °C can

be obtained in only 4 minutes. Also sintering time is reduced in SPS due to small holding time at sintering temperature, usually 5 to 10 minutes. In SPS, since no coarsening and grain growth were allowed to occur, high relative densities were reached in very short time and nano sized powders can be sintered without considerable grain growth. Hence, nano-structured ceramics or nanocomposites can be easily prepared by SPS having higher density and fewer defects. These nano-structured composites exhibit excellent mechanical properties like high strength, high hardness etc. *Ricote* demonstrated a single phased and high $BaZr_{0.9}Y_{0.1}O_{3-\delta}$ pellet has been obtained by spark plasma sintering, with a 5 min dwell at 1700 °C.[28]

(e) Cold sintering

Most sintering processes occur at high temperatures>1000 °C. Cold sintering process (CSP) is an extremely low-temperature sintering process (room temperature to ~200 °C) that uses aqueous-based solutions as transient solvents to aid densification.[29] In conventional high-temperature sintering processes, individual ceramic powder particles densify into a dense object. The driving force for this process is the reduction of the high surface free energy of the powder by material diffusion which only occur at high temperatures. Whereas cold sintering relies on interfacial solution effects in water for the densification of the materials – a process that occurs at low temperatures and over much shorter time when pressure is applied. Guo et al demonstrated the applicability of CSP to improve the green density of 8Y-YSZ ceramics.[30] *Berbano* obtained 80% dense $Li_{1.5}Al_{0.5}Ge_{1.5}(PO_4)_3$ electrolytes at 120 °C in 20 minutes.[31] Preparation of dense proton conductor has not been reported so far. Maria *et al.*[32] proposed an initial model for cold sintering that comprises two stages : an initial stage is predominated by mechanical forces and particle rearrangement, and a second stage is predominated by pressure/temperature-assisted dissolution and precipitation events that driven by local and global gradients within the pellet die.

4.1.3 MATERIALS CHARACTERIZATION

Phase composition and microstructure

X-ray diffraction (Rigaku TTR-III) analysis was used to examine the phase purity of the powders with Cu Kα radiation source. The XRD patterns were obtained in the range of 20°-80° with a 0.02° step size and a scan speed of 0.5 °/min at 40 kV and 200 mA. The microstructure and morphology of the BZY20, BCZYYb and TiO_2 pellets were revealed by using scanning electron microscopy (SEM). The catalyst nanoparticle distribution was estimated by the element distribution as observed by EDS.

Electrochemical Impedance Spectroscopy (EIS)

The measurement of ionic conductivity due to the motion of hydrogen/deuterium ions through these materials gives fundamental information regarding the ion transport properties and allows for the exciting possibility of isotope separation using these oxides a separation membrane. The electrochemical properties of ceramic pellets were measured using the symmetrical cells. Silver paste was printed on both sides of the pellet to form a symmetrical cell, Ag/pellet/Ag, in which Ag layer worked as electrodes. EIS measurements were performed under air. Impedance spectra were acquired using a Solartron 1260 electrochemical workstation with an AC amplitude of 10 mV in the frequency range from 5M Hz to 0.1 Hz. AC impedance plots were fitted using Zview software according to the equivalent circuit with a standard deviation below 5%. Impedance can be expressed as $Z = Z' + j*Z''$, in which Z' is the real part

and the Z'' is the imaginary part, and j is the square root of -1. The plot of Z'' versus Z' is called a Nyquist plot. The EIS is one of the most promising methods for unfolding complex electrochemical systems and has proven to be a powerful tool in investigating different polarization processes in solid oxide fuel cells and other electrochemical systems such as gas separation membranes.

Thermogravimetric analysis (TGA)

Samples were cut out from the pellets for TGA experiment which was performed using STA 449 F3 Jupiter (ZETZSCH). The detailed pretreatment condition and temperature program will be given in the results section.

Raman measurement

The measurement of the Raman spectra was done by Raman instrument from Horiba with TS1500 hot stage (shown in Figure 4.1). The Raman shift ranges from 2000 cm^{-1} to 4000 cm^{-1} under 3%H_2O or D_2O humidified air.

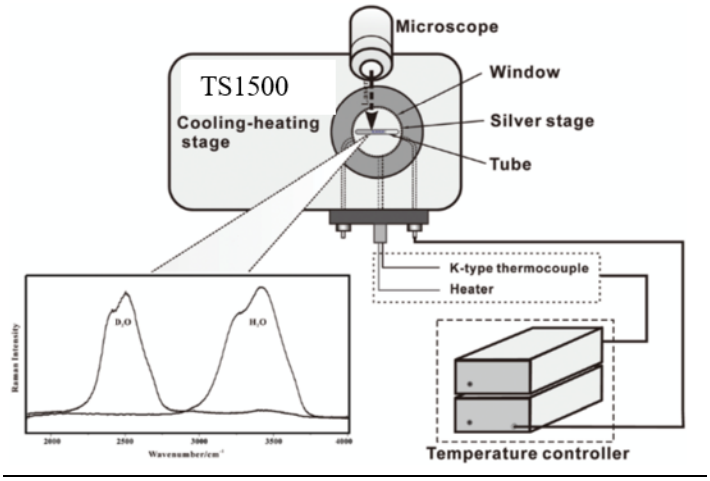


Figure 4.1. The schematic of the Raman experiment system.

4.2 RESULTS AND KEY FINDINGS

4.2.1 SIMPLE OXIDES: COLD SINTERING OF TiO_2

Here we constructed a home-made cold sintering device to perform our experiment. We used normal harden carbon steel die set, the heating tape with a temperature controller as the heating source, and hydraulic press as force source to create appropriate temperature and pressure conditions for cold sintering process, which shown in Figure 4.2. A schematic evolution of a powder compact process during cold sintering is shown in Figure 4.3. Normally, we have two methods to introduce water into the powder, one is by storing the powders or pellets in a constant relative humidity for 10-360 min. TiO_2 powders (anatase phase, 25nm, 99.9% purity) were purchased from commercial source (Inframat Advanced Materials), the raw powders were mixed with 30wt% deionized water using pestle and mortal for 1-2 min. The mixture was uniaxially pressed under 350MPa first at room temperature (25℃) for 10min, and then the

temperature increases to 120℃. The temperature was kept for an hour to obtain an TiO_2 membrane. The acquired membranes were baked at 200℃ overnight to remove possible water.

Then we used the Archimedes method to test the relative density of the pellets. By weighing the dry weight m_1, immersed weight m_2 (sample is immersed in water) and soaked weight m_3 (sample is taken out of the boiling water and wiped with paper), we calculated the Archimedes density.

$$q=\frac{m_2-m_1}{m_2-m_3}\times 100\%$$

The relative density of cold sintered TiO_2 pellet is about 73.8 %, which is much higher than the pellet made by uniaxially pressure at 350MPa.This TiO_2 pellet sample was further characterized by SEM and the images for the surface and cross are shown in Figure 4.4. The grains after cold sintering have an elongated shape. However, the grain size of the TiO_2 after cold sintering is similar to that TiO_2 before cold sintering, which implicates that this method can avoid the grain growth for forming a nanostructured membrane with nano-size grain boundary and nano-pores. The proton transport behavior will be further measured by conductivity and isotope exchange test in the next stage of the project.

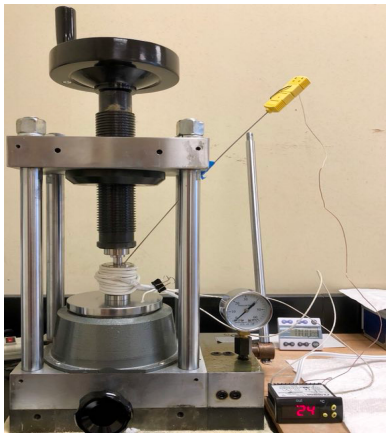


Figure 4.2 Photograph of cold sintering press with heat controller on conventional pellet die

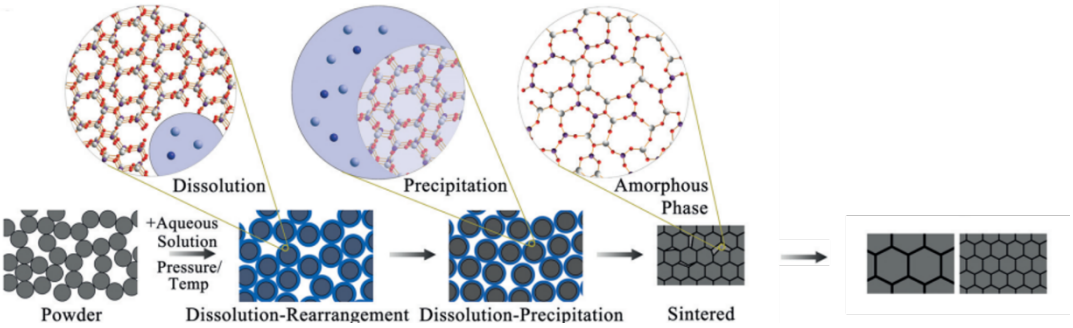


Figure 4.3 Schematic evolution of a powder compact process during cold sintering[3, 4]

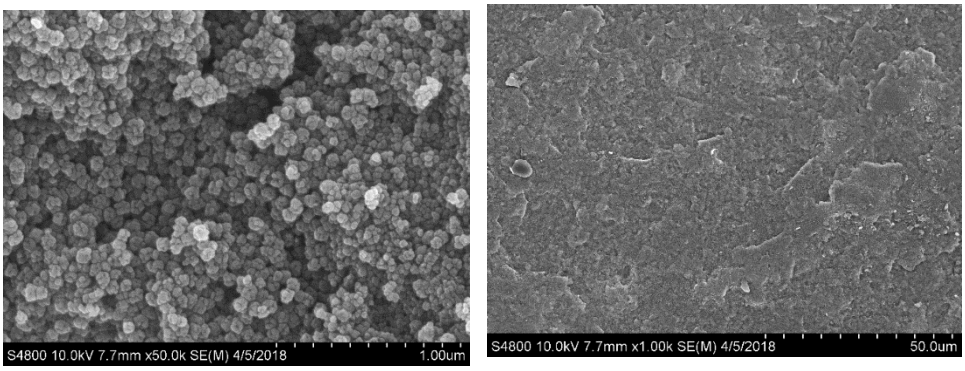


Figure 4.4 SEM of cross section and surface TiO_2 pellets after cold sintering

4.2.2 SIMPLE OXIDES: TRADITIONAL SINTERING OF TiO_2

The traditional sintering method was employed to fabricate nanoscale TiO_2 membranes. Nano TiO_2 powders were pressed in a stainless die at 150 MPa and then sintered at 700 ºC for an hour. The temperature was chosen to avoid the phase transition from the anatase phase to the rutile phase which occurs at is 750 to 800 ºC. The Anatase phase of TiO_2 was targeted due to it's demonstrated high catalytic activity. The short dwell time was selected to avoid the grain growth of the nano-powder resultsing in a nano-structured membrane.

The crystal structure for the TiO_2 membrane was evaluated by X-ray diffraction with Cu-Kα radiation and is summarized in Figure 4.5. The raw TiO_2 nanoparticles used in this project was the anatase phase, and there was no phase change observed after heat trreatment except for some minor changes in the peak density after traditionl sintering at 700 ºC for an hour.

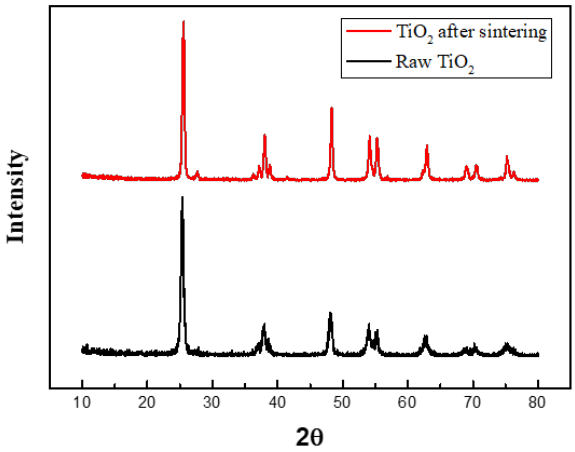


Figure 4.5. XRD patterns of fresh TiO_2 powder and TiO_2 pellets obtained by traditional sintering at 700 ºC for 1h

The particle size and morphology of the nanostructured TiO_2 membrane was examined by SEM, as shown in Figure 4.6. The raw particle size of the TiO_2 powder acquired from the company was approximately 25 nm; there is a slight increase to 30 ~ 40 nm after sintering. This work demonstrates the parameters

used in traditional sintering could inhibit the grain growth of the nanostructured titanium dioxide membrane.

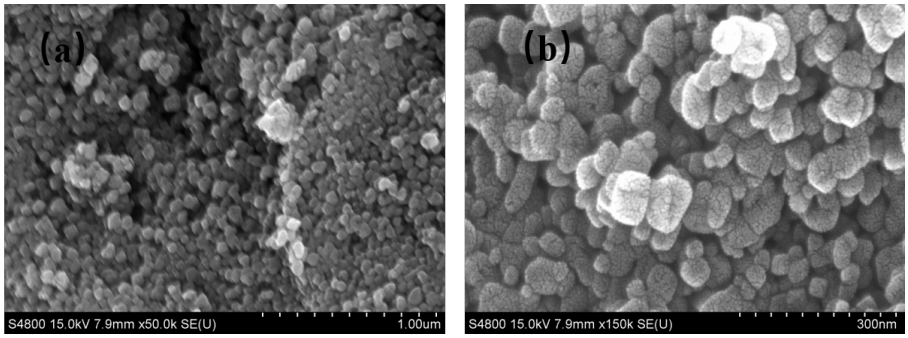


Figure 4.6. SEM image of the cross-section of TiO_2 pellets after traditional sintering a) low magnification and b) high magnification

TGA was used to analyze the water absorption and de-absorption process in the nanostructured membrane. Firstly, we increased the temperature to 600 ºC and dwelled for one hour in a protective atmosphere (argon). In this process, we tried to remove all the gas molecules and absorbed water from the sample. Secondly, we decreased the temperature to room temperature in wet (D_2O) nitrogen to accomplish the water absorption process. The sample was then re-heated to 250 ºC to observe the water loss from the material. 250 ºC was selected due to the point where the activation energy exhibits a change in slope as discussed above. Figure 4.7 displays the results of TGA. Water absorption occurs with decreasing temperature, with nearly 0.8 wt.% (compared to the sample) water absorbed in this process. Nearly 80% of the absorbed water was lost during the subsequent heating step to 250 ºC. The high proton conductivity discussed below could be explained by the strong uptake of water at low temperatures.

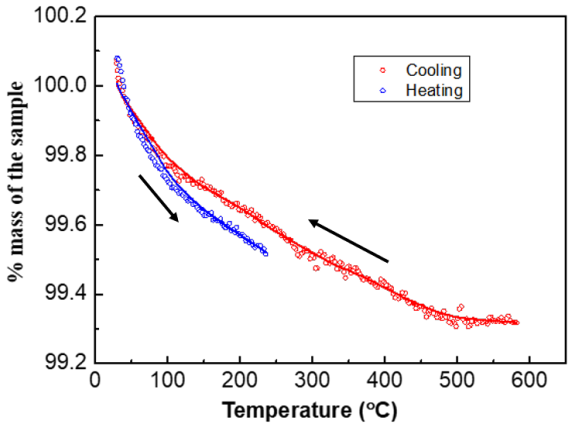


Figure 4.7 Hydration behavior of the nanoscale TiO_2 membrane obtained from thermo-gravimetric analysis

The H/D isotope exchange effect and proton conductivity were determined by EIS. The representative EIS spectra for the TiO_2 membranes in the wet H_2O and D_2O are shown in Figure 4.8. The protonic nature of the conduction in a humid atmosphere is evidenced by the presence of an evident isotopic effect when gas saturated with D_2O is used. The nanoscale TiO_2 membrane has lower resistance in wet H_2O than that in D_2O, indicating the hopping mechanism of proton transport at low temperatures.

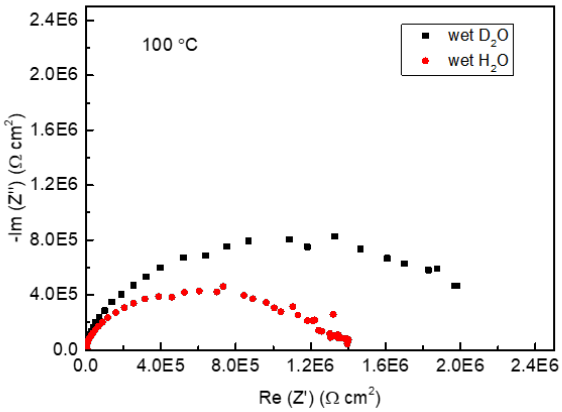


Figure 4.8. The representative EIS of the porous TiO_2 membrane in wet (H_2O and D_2O) air

Figure 4.9 shows the conductivity of the TiO_2 membrane in wet (H_2O or D_2O) and dry air. At high temperatures, proton conductivity decreases with the decreasing the temperature both in the wet and dry air. While at low temperatures in wet air, the conductivity increases with the decreasing temperatures, which reflects the intra-grain conductivity caused by the absorption of water in the nanoscale membrane. The point at which the activation energy changes slope in wet air is 200 to 250 ºC. The proton conductivity in wet (H_2O) is slightly larger than that in the wet (D_2O) with a factor of approximately 2, which is close to the theoretical value of 1.4, signifying hopping-based conduction of protons with the conductivity determined by the mass of the ionic species. However, in dry air, there was no activation energy change with decreasing temperature observed, also at low temperatures, the bulk resistance is too large to determine the accurate conductivity from EIS methods.

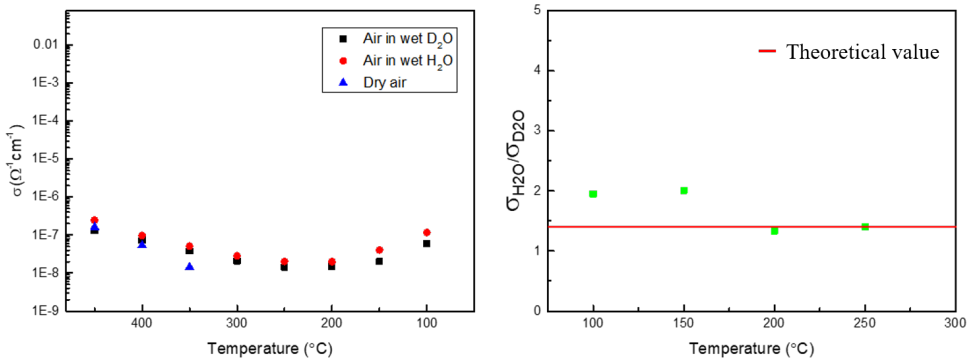


Figure 4.9. a) Total conductivity of porous TiO_2 in dry and humidified air (H_2O and D_2O) and b) the ratio (σ (H_2O)/ σ(D_2O)

In summary, the increased conductivity of nanostructured TiO_2 membrane in a wet atmosphere and its polarization behavior confirm the existence of proton conductivity in the nanoscale TiO_2 membrane at low temperatures (< 250 ºC). The difference of proton conductivity in H_2O and D_2O reveals the hopping mechanism of the proton conduction. In addition, the thermogravimetric analysis reveals strong water uptake below 250 ºC which help explains the high proton conductivity at low temperatures.

4.2.3 Insights into the proton transport mechanism in TiO_2 simple oxides by in-situ Raman spectroscopy

Porous TiO_2 membranes were fabricated by a traditional sintering method. Nanoscale TiO_2 powders were pressed in a stainless die at 150 MPa and then sintered at 700 °C for an hour in ambient air to form porous nanocrystalline pellets. Dense membranes were prepared by spark plasma sintering (SPS) method. Powders were filled into a graphite die and sintered by SPS (Dr. Sinter 1020, Sumitomo Coal Mining Co.). This process was accomplished by applying a constant 5 KN axial force and an increasing current (100 A/min) simultaneously to the die in dynamic vacuum (~10 Pa).

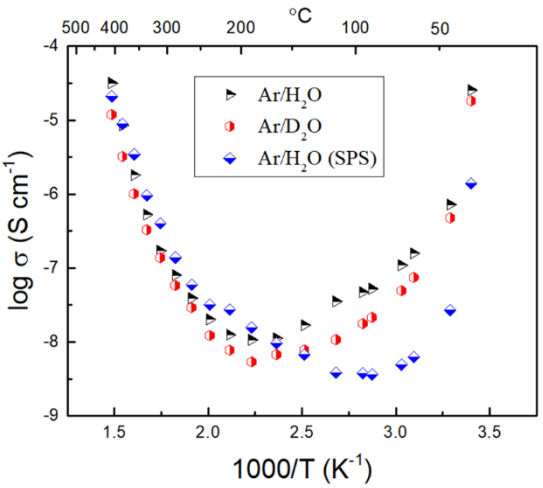


Figure 4.10. Total conductivity of porous TiO_2 membrane under Ar-H_2O, Ar-D_2O and dense TiO_2 membrane fabricated by SPS method under Ar-H_2O.

Figure 4.10 shows the electrical conductivity of the as-prepared TiO_2 membrane exposed to different environments and temperatures. The conductivity generally increases with increasing temperature above 150 °C where proton transport occurs predominantly in the chemisorbed water layer. With decreasing temperature, the activation energy gradually decreases, and the conductivity shows a thermally deactivated nature below 150 °C. Total conductivity increases with the decreasing temperature where proton transport in the hydrogen-bonded layer. All observations agree with previous reports of proton conduction in porous ceramics.[10] A clear isotopic effect occurs when gas of Ar-D_2O was used. The conductivity in Ar-H_2O is clearly higher than that in Ar-D_2O, with approximately ($\sigma(H_2O)/\sigma(D_2O)$) ratio around 2, closing to the theoretically value 1.4, suggesting hopping-based proton conduction on oxides' surface and grain boundary interfaces.

In-situ Raman was executed to confirm the OH and OD vibrations on the oxides' surface. The first chemisorbed layer above oxides' surface consists of terminated and multi-coordinated hydroxyls, followed by additional molecules subsequently adsorbed on the hydrogen-bonded water molecules.[34] Representative Raman spectroscopy results of OH and OD vibrations measured from 25 to 300 °C are shown in Figure 4.11. The OH vibration appears at ~ 3400 cm^{-1} with a shoulder at 3200 cm^{-1} and the OD vibrations appears at ~ 2550 cm^{-1}. Also, with increasing temperature, (1) the intensity of OH and OD vibrations decreased due to the reduced water absorption; (2 the main peaks shifted to higher

wavenumbers, and (3) the width of the peaks were largely reduced, in agreement with previously reported spectra of OH and OD stretch band profiles.[35]

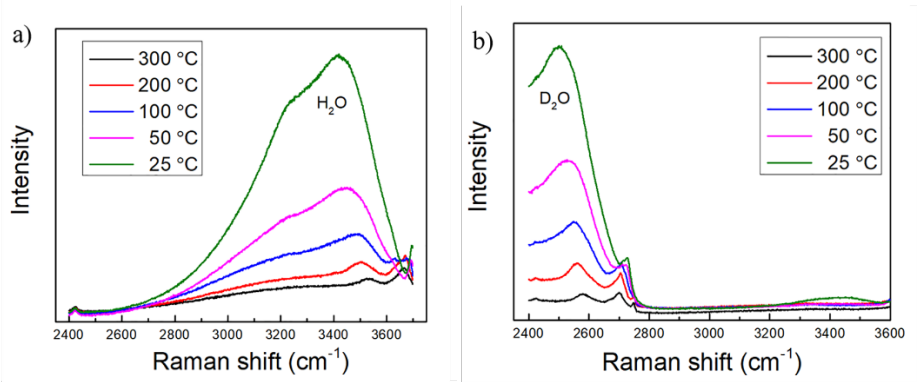


Figure 4.11. The representative OH (a) and OD (b) Raman vibration from 25 to 300 °C under Ar-H_2O and Ar-D_2O, respectively.

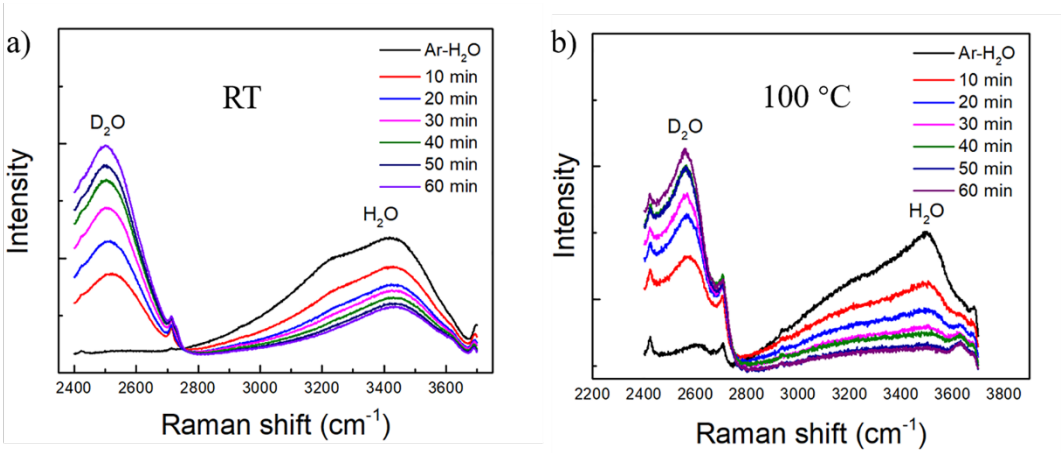


Figure 4.12. Temporal evolution of Raman spectra of TiO_2 membrane after switching the atmosphere from Ar-H_2O to Ar-D_2O at (a) room temperature and (b) 100 °C.

The exchange reactions of H_2O and D_2O were also studied by *in-situ* Raman spectroscopy toward gaining insight into the proton transport mechanism. Spectra time evolution is shown in Figure 6 where representative spectra in the range of 2400-3700 cm^{-1} are presented. These spectra were obtained after switching the atmosphere from Ar-H_2O to Ar-D_2O at room temperature and at 100 °C. The O-H vibration immediately starts attenuating after the addition of D_2O to the atmosphere as illustrated by changes to the ν_{OH} broad band at ~ 3400 cm^{-1} and the ν_{OD} broad band at ~ 2550 cm^{-1} due to the isotope exchange reactions of hydroxyl groups on the oxides' surface, suggesting the Grotthuss mechanism. The O-H vibration almost disappears after 30 minutes at 100 °C, indicating a fast isotope exchange rate at 100 °C than room temperature.

During the OH/OD exchange, the relevant variable is the fraction of remaining OH, which is experimental determined in terms of ratio $I_{OH}/I_{OH\ \mathrm{Initial}}$. As shown in Figure 4.13 (a), the decrease in the ν_{OH} integrated intensity follows a straight line in the semi-logarithmic plot. It is therefore possible to define a first order rate constant, $k_{H/D}$ as described in Amado and Da Silvia's report.[36,37] Temperature dependent measurements indicated the exchange rates were appreciably faster at elevated temperatures. In a plot of

Ln(k) *vs*. 1/T, linear correlations were obtained for the isotope exchange reactions from Ar-H_2O to Ar-D_2O, suggesting Arrhenius-type dependence of the rate constant. The resulting activation energy, E_a, of 9 kJ mol^{-1} was determined for the H/D exchange on nanoscale oxides' surface and grain boundary interfaces.

Table 4.1 displays a summary of H/D isotope exchange coefficient (k) and activation energy (E_a) in different material systems. The activation energy E_a for H/D exchange found in this work, which is lower than the reported activation energy, 26 kJ/mol for H/D exchange in β-cyclodextrin dodecahydrate, indicates H/D exchange reactions occur more easily on the absorbed water of oxides' surface than hydroxyl group in β-cyclodextrin dodecahydrate. The activation energy is comparable with noble metal system for the D_2/H_2 exchange reactions. Interestingly, the surface exchange coefficient (k) in nanoscale simple oxides is 100 times higher than that in the traditional oxidic proton conductor

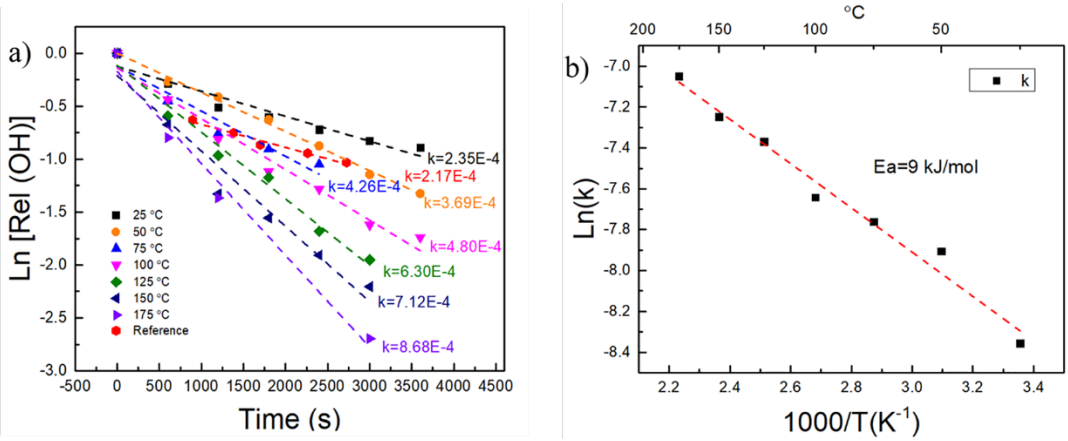


Figure 4.13. (a) Natural logarithm of the integrated relative Raman v_{OH} intensity in porous nanostructured TiO_2 membrane, as a function of time of exposure to an atmosphere of Ar-D_2O together with the isotope exchange rate in β-cyclodextrin dodecahydrate[37]; and (b) Ln(k) *vs*. 1/T for H/D isotope exchange reactions on oxides' surface.

Table 4.1. A summary of H/D isotope exchange coefficient (k) at room temperature and activation energy (E_a) in different systems.

Exchange	Materials	Surface exchange rate (k)	Activation energy (E_a)	Method	Reference
D_2O/H_2O	TiO_2	2.35 e^{-4} s^{-1}	9 kJ/mol	*In-situ* Raman	This work
D_2O/H_2O	$SrCe_{0.95}Yb_{0.05}O_3$	1.4 e^{-6} s^{-1}	--	Elastic recoil detection (ERD)	[38]
D_2O/H_2O	β-cyclodextrin dodecahydrate	2.17 e^{-4} s^{-1}	26 kJ/mol	*In-situ* Raman	[37]

D_2/H_2	β phase -- Palladium	3.5, 25 kJ/mol	Residual gas analyzer (RGA)		[39,40]

($SrCe_{0.95}Yb_{0.05}O_3$).[38] It is noted that this material was prepared by solid state reaction method with large grain size resulting in negligible water absorption on the surface and grain boundary interfaces. This indicates proton mobility at the surface and grain boundary interfaces in nanoscale simple oxides system is much higher than the "bulk effect" of traditional proton ceramic conductors at room temperature, which is consistent with the reported phenomenon in nanoscale cerium oxide system.[41] From TGA data, we know that the nanoscale TiO_2 membrane can absorb 0.03 mol water per mol TiO_2. If it is assumed that (i) the entire water content is absorbed on the surface and grain boundary interfaces and (ii) the monolayer water layer thickness is 0.282 nm,[42,43] according to the BET data, the surface and grain boundary interfaces can accommodate ~ 10^{22} protons cm^{-3}. Therefore, the estimated surface concentration of protons is comparable to the calculated bulk content of protons derived from typical dopant concentration (*i.e.* 15 mol% yttrium-doped $BaZrO_3$ has a proton concentration of ~10^{21} protons cm^{-3}), of typical high temperature proton ceramic conductors found in literature.[41]

Clearly, water absorption on the surface and grain boundary interfaces in simple oxide systems has higher proton mobility and similar proton concentration as compared to the traditional high temperature proton ceramic conductors. Notably, the conductivity (σ, S/cm) follows equation 3, of which n is carrier density (# of carriers/cm^3), q is the electric charge (C) and μ is the mobility (cm^2/Vs), suggesting 3 orders higher of interfacial conductivity as compared to the low conductivity transport in high temperature proton ceramic conductors through the bulk and then across the grain boundaries at low temperatures.[41]

$$\sigma = nq\mu \tag{3}$$

Figure 4.14 shows the water structure on nanoscale oxides' interface[44] and hydroxyl defects[45] in the perovskite structure under humidified atmosphere. These results indicate that when the grain size of proton ceramic conductor is decreased, this will provide more active sites on the surface or grain boundary interfaces for water absorption, resulting in improved proton transport properties by combining the known "bulk effect" (hydroxyl defects) and newly discovered "interface effect" (absorbed water) in Zone 2 (50 °C < T < 150 °C). This combination of effect results in conductive interfaces which enhance ionic transport instead of blocking transport which provides a new promising solution for the development of a new generation of proton ceramic conductors at low temperatures.

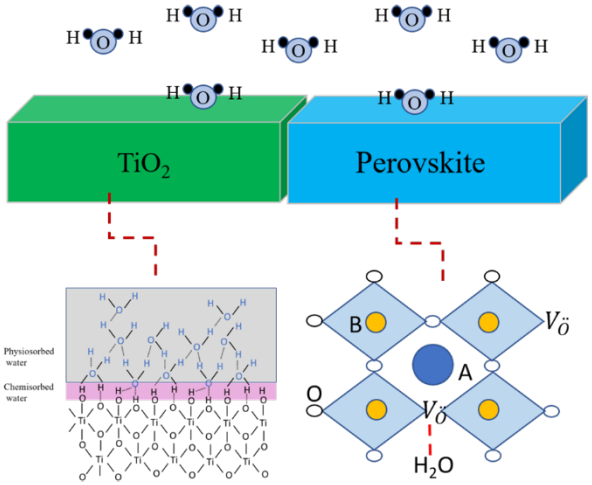


Figure 4.14. Illustration of the water structure on nanoscale simple oxides' interface and hydroxyl defects forming in perovskite structure under humidified atmosphere.

In summary, *in-situ* Raman spectroscopy was used to directly identify the proton transport mechanism on the interface of nanostructured ceramic membranes. The observed isotope exchange reactions on the interface indicates a Grotthuss or "hopping" type mechanism of proton transport which is selective isotopes based on mass. Fast isotope exchange reactions with an activation energy of 9 kJ mol^{-1} for H/D exchange on oxides' surface were observed in simple oxides which was over 100 times higher than the traditional oxidic proton conductors. In addition, the estimated surface concentration of protons in simple oxides is comparable to the calculated bulk content of protons for typical perovskite based protonic conductors indicating the potential for enhanced conduction. Based on these results new materials systems are proposed which combine surface and bulk effects in an intermediate temperate range resulting in a promising new solution for the development advanced ionic conductors through interfacial engineering at the nanoscale.

4.2.4 PEROVSKITE OXIDE MATERIALS: COLD SINTERING OF BZY20

The perovskite material $BaZr_{0.8}Y_{0.2}O_{3-\delta}$ (BZY20) nano-powders synthesized by the modified Pechini method was chosen as a model system for the cold sintering process. Experiments were conducted by mixing ~0.8 g powders with a proper amount of water and dry-pressed under ~400 MPa for 10 minutes in circular carbon-aided steel die set with a diameter of 1/2 inch (12.7 mm). The die set was heated to 180 ºC and hold for 1 hour to obtain a BZY20 pellet. The pellet was placed in the box furnace overnight at 120 ºC to completely remove residual water. A final sintering process was utilized to get a porous BZY20 pellet. Thus, water amount and final sintering process are two key factors, which affect the microstructure of pellets.

Effect of sintering temperature

The influence of the sintering temperature and sintering time were investigated. 20 wt% water was selected as the water amount, and pellets were sintered at 1350 ºC and 1450 ºC for 12 h or 24 h, respectively.

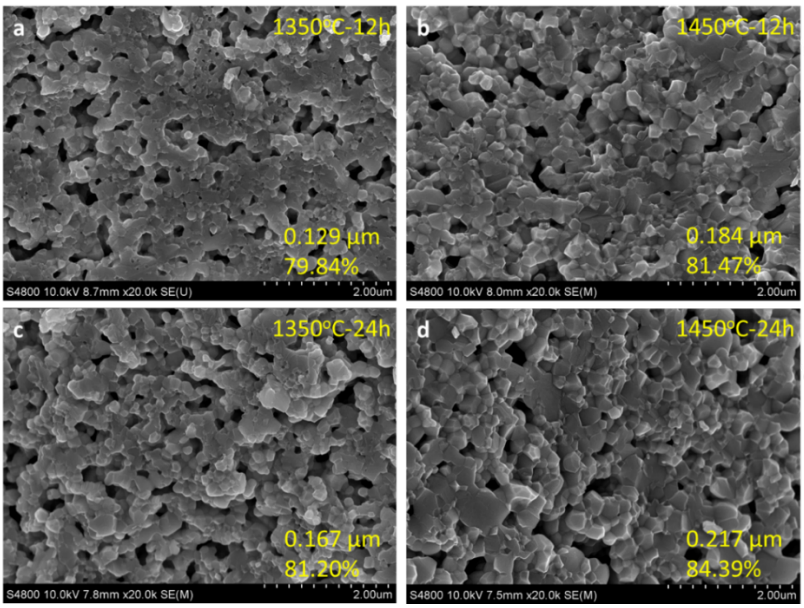


Figure 4.15. SEM images of BZY20 pellet's cross-sections which were sintered at (a) 1350 ºC for 12 h, (b) 1450 ºC for 12 h, (c) 1350 ºC for 24 h and (d) 1450 ºC for 24 h. (Average grain size and relative density calculated by images are inserted at bottom right corner for each image.)

Based on Figure 4.15, both higher sintering temperature and longer sintering time result in larger grain size and higher relative density. Because relative densities were calculated based on images, they are a little higher than those obtained from measurements of geometrical density. From these results we could conclude that a lower sintering temperature is better for obtaining uniform grain sizes with lower relative density.

The effect of water content

Different water amounts were used to densify BZY20 nano-powders. 20 wt% and 30 wt% water was selected to synthesize BZY20 pellets, respectively.

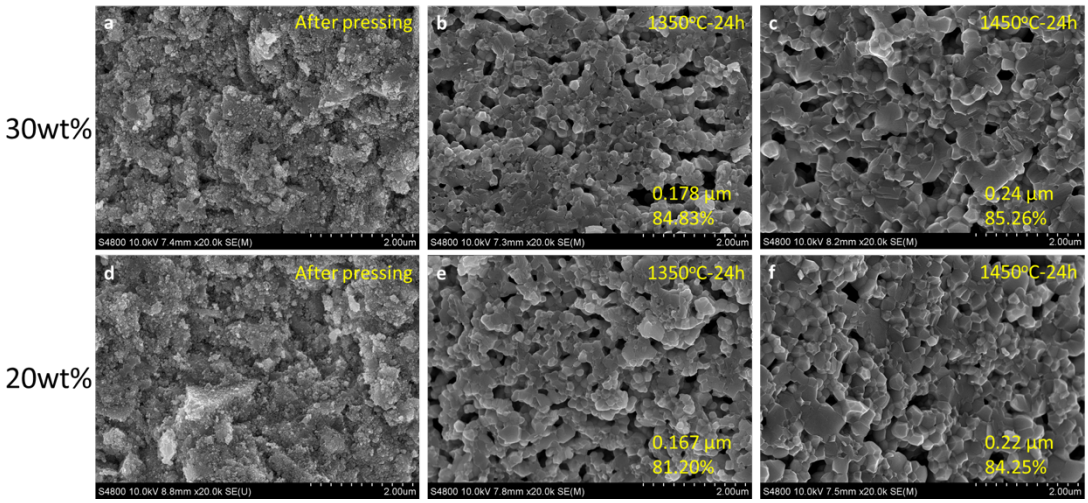


Figure 4.16. SEM images of BZY20 pellet's cross-sections with different water amount. (a) 30 wt% water after pressing, (b) 30 wt% water sintered at 1350 ºC for 24 h, (c) 30 wt% water sintered at 1450 ºC for 24 h, (d) 20 wt% water after pressing, (e) 20 wt% water sintered at 1350 ºC for 24 h and (f) 20 wt% water sintered at 1450 ºC for 24 h. (Average grain size and relative density calculated by images are inserted at bottom right corner for each image.)

As shown in Figure 4.16, samples prepared with different water amounts resulted in similar cross-section views. However, after firing under proper conditions, noticeable difference was observed. In brief, higher water concentration results in a larger grain size and higher relative density. The effect of sintering process and water amount were discussed based on our sintering results. These effects of tailored porosity may be benefecial for our further applications in this project.

Figure 4.17 summarizes the XRD patterns for the BZY20 green pellets after traditional dry pressing and cold sintering before the final sintering at 1500ºC. The XRD plot for the BZY20 precursor indicates the prescence of minor $BaCO_3$ peak exists in the BZY20 precursor powder synthesized using the modified Pechini method with an eventual calcination temperature of 900ºC. For calcining the BZY20 powder, the calcination temperature lower than 950ºC or the inefficient air exchange in the box furnace usually resulted in a residual amount of $BaCO_3$ phase inside the BZY20 powder. In this work, the use of a low calcination temperature of 900ºC helped achieve BZY20 powder with a smaller particle for improving BZY20's sinterability. The BZY20 green pellets, after the pretreatment of traditional pressing and cold sintering without water (TS-0 and CS-0), maintained a cubic perovskite structure with a similar $BaCO_3$ peak intensity. However, the addition of 20wt% of water for both traditional pressed and cold sintered BZY20 green pellets (TS-20 and CS-20) increased the peak intensity of $BaCO_3$. Pretreatment with 20wt% H_2O addition resulted in the formation of a distinct $BaCO_3$ phase. The previous studies indicated that a proper amount of $BaCO_3$ in BZY20 could improve the BZY20's sinterability to achieve high relative

density and large grains [46]. Therefore, we expect that the introduced $BaCO_3$ in BZY20 by the pretreatment with 20wt% can increase the sintered BZY20 pellets' relative density.

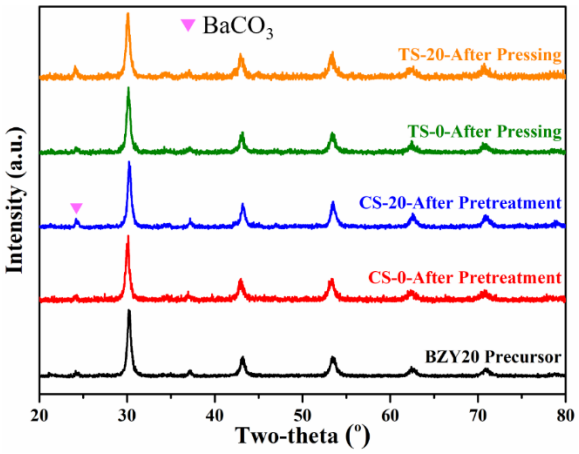


Figure 4.17. XRD patterns of BZY20 precursor powders and green pellets after cold sintering pretreatment and traditional pressing process with different water amounts.

The green histograms in Figure 4.18 provide the relative densities of the BZY20 green pellets. The CS-20 BZY20 green pellet after cold sintering with 20wt% water at 180°C showed a relative density of ~76%, which was higher than the theoretical packing density of the cubic close-packing structure (~74%) based on equal spheres. The three other BZY20 green pellets of CS-0 (cold sintering without water), TS-0 (traditional pressing without water), and TS-20 (traditional pressing without 20wt% water) showed relative densities much lower than the one for CS-20 green pellet (53-56% vs. 76%). Since the high relative density for the green pellets usually resulted in high relative density for the sintered pellets, we expect to achieve high relative density for the BZY20 pellets pretreated by cold sintering with 20wt% at 180°C.

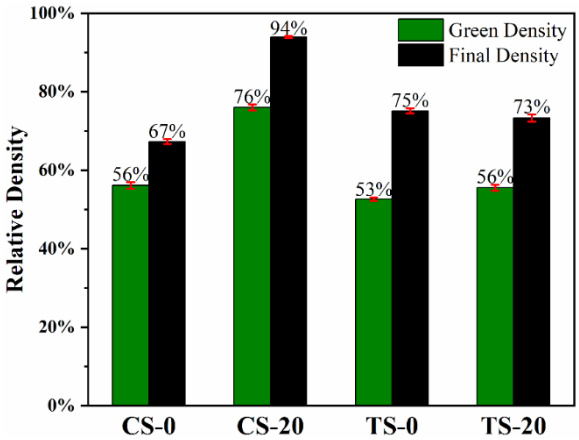


Figure 4.18. The summary of relative densities (calculated by the geometric measurement) for all samples discussed.

Figure 4.19 further provides the cross-section SEM images of the BZY20 green pellets cold sintered at 180ºC with and without water. The BZY20 green pellets cold sintered with 20% water (CS-20, Fig. 3b) showed a homogenous and highly compacted microstructure consistent with the high green relative density (Fig. 2, CS-20). The BZY20 green pellets cold sinter without water (CS-0, Fig. 3a) showed an inhomogeneous and loosely packed microstructure consistent with the low green relative density (Fig. 2, CS-0). In summary, the CS-20 BZY20 green pellets cold sintered with 20wt% water at 180ºC showed the proper amount of $BaCO_3$ as a sintering aid, high green relative density, and homogeneously compacted microstructure. Therefore, we expect to achieve improved sinterability for BZY20 green pellets cold sintered with 20wt% water at 180ºC (CS-20 BZY20 green pellets).

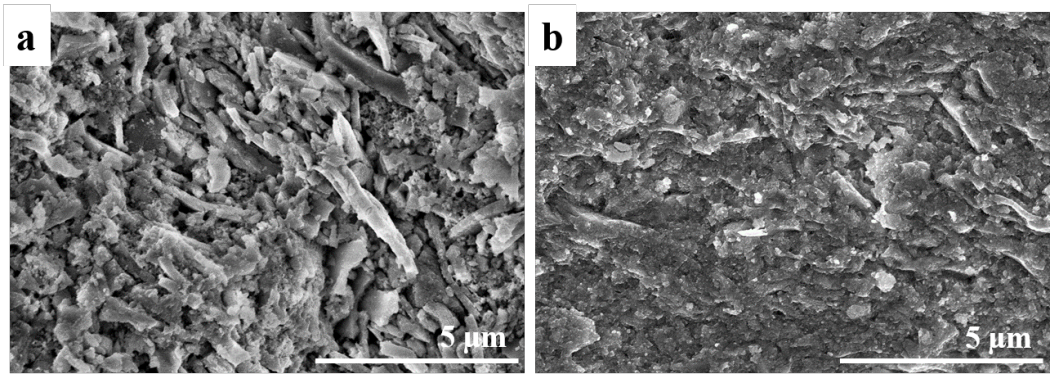


Figure 4.19. The cross-sectional SEM images of CS-0 (a) and CS-20 (b) after cold sintering pre-treatment.

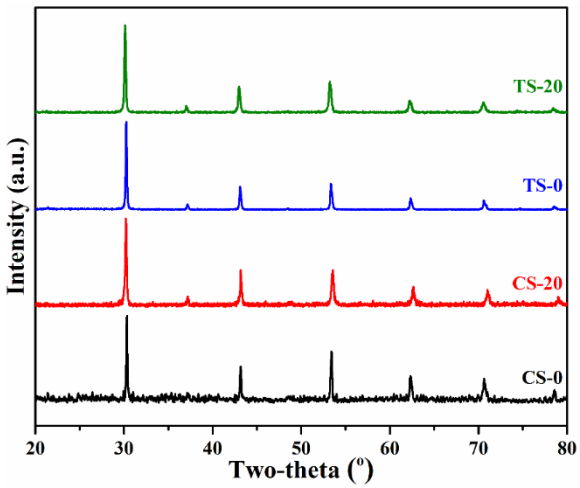


Figure 4.20**.** XRD patterns of BZY20 pellets that fabricated with the cold sintering pre-treatment and the traditional sintering method with different water amounts.

Figure 4.20 summarizes the XRD patterns for the BZY20 pellets sintered at 1500ºC for 12 h. The XRD patterns indicate that all the four sintered BZY20 pellets formed the pure cubic perovskite structure with a space group of $Pm\bar{3}m$ with $BaCO_3$ impurity completely disappeared. The relative intensity, width, and position of the corresponding peaks for all four samples do not show a

noticeable difference, which indicates crystal structures of the sintered BZY20 under different conditions was the same within our XRD analysis error range. In other words, different pretreatment conditions (Table 1) for the BZY20 green pellets did not affect the eventual crystal structure of a fully sintered BZY20 pellet, which ensured good proton conduction properties.

The black histograms in Figure 4.18summarize the relative densities of the BZY20 pellets after the subsequent sintering at 1500ºC for 12 h. The CS-0, TS-0, and TS-20 BZY20 pellets after sintering resulted in much lower relative densities of 67%, 75%, and 73%, respectively. Considering the lower green relative densities and the less $BaCO_3$ sintering aid for CS-0 and TS-0 BZY20 green pellets, the poor sintering results for these three samples are reasonable. After a longer pressing process and higher temperature, even the density of CS-0 was higher than TS-0. The inhomogeneous microstructure discussed above eventually leads to a much lower relative density after the final 1500ºC sintering (~67%) than TS-0. For TS-20, the addition of 20wt% H_2O might somehow help to improve the packing density after 10 min pressing comparing with TS-0. Once the final 1500ºC sintering was conducted, the extra water just went without leaving any improvement as showing the similar relative density with TS-0 considering the experimental error (red bar in Fig. 2). In other words, the additional 20wt% H_2O in the room temperature pressing does not affect the final relative density even though it may lead to a little bit of improvement for the density of green pellet. When cold sintering was applied, the added water could strongly interact with BZY20 powders rather than simple physical absorption. The CS-20 BZY20 pellets achieved a relative density as high as ~94% after the final sintering, consistent with its high green relative density, homogeneous and compact microstructure, and a larger amount of $BaCO_3$ sintering aid.

Figure 4.21 summarizes the fractured cross-sectional SEM images for all the four BZY20 pellets after sintering at 1500ºC for 12 h. The CS-20 BZY20 pellet does not show any obvious pores suggesting the high relative density. All the other three BZY20 pellets (CS-0, TS-0, and TS-20) show visible pores in the SEM micrographs in line with the low relative densities reported above. The further comparison of these four pellets' microstructures indicates that the sintered CS-20 pellets have grain sizes ~1μm, almost twice those for the other three samples. Therefore, we can conclude that the cold sintering pretreatment with 20wt% water at 180ºC for 1 h can efficiently assist the sintering process of the BZY20 pellets, which allowed the densification of the refractory BZY20. The densification temperature was lowered by about 200ºC compared to the traditional sintering method. The fully densified and large-grained microstructure should result in high proton conductivity.

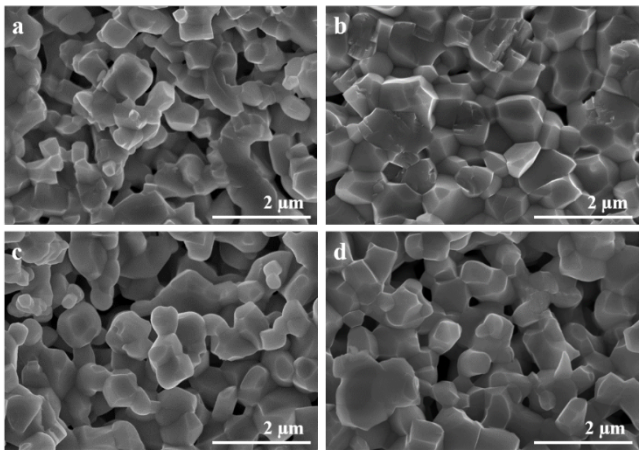


Figure 4.21. The cross-sectional SEM images of CS-0 (a), CS-20 (b), TS-0 (c) and TS-20 (d).

Figure 4.22 presents an exemplar EIS spectrum measured at 300°C under wet air condition for the symmetrical cell comprised of the sintered CS-20 BZY20 electrolyte and silver electrodes. The red square points show the Nyquist plot of EIS measurement results after area normalization. As is shown, the Nyquist plot consists of an intercept at the Z-Real axis at high frequency, two depressed small semicircles at intermediate-frequency range, and a straight line with ~45 degrees relative to the Z-real axis at low-frequency range. The equivalent circuit model (inset in Fig. 6) was used to fit the EIS data points by Z-View software. For detail, the consisting of the elements of electrolyte bulk, electrolyte grain boundary, electrolyte-electrode interfacial charge transfer (protons), and electrode diffusion, The EIS Nyquist plots' analysis is the same as most protonic ceramic electrolyte symmetrical cells, allowing the achieving of electrolyte electrical conductivities quickly. The characteristic frequencies (f_{max}) and capacitance (C) are listed in Fig. 6, which fall in the similar value literature reported [47].

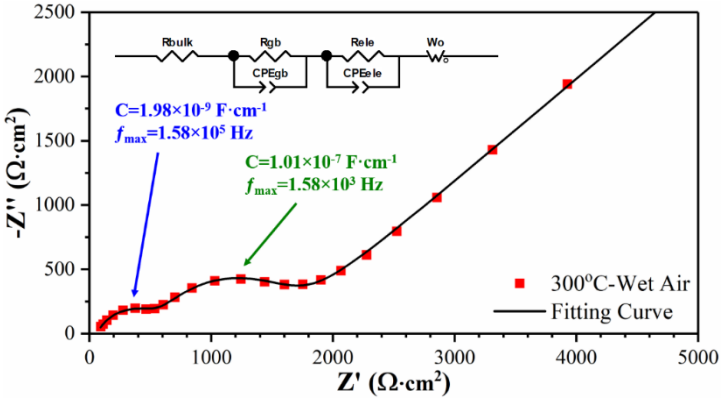


Figure 4.22. The fitting of the EIS plot of the CS-20 sample was tested at 300°C under wet air. Inset is the equivalent circuit used for fitting.

Figure 4.23 displays the total conductivities of the CS-20 BZY20 under different atmospheres (dry air, wet air, dry 5% H_2, and wet 5% H_2) in the temperature range from 300°C to 700°C. It is consistent with most other reports that our BZY20 electrolyte pellets showed increased total

electrical conductivities with increased temperature. The atmospheres showed a significant effect on the electrical conductivities at a specific fixed temperature. The total conductivities under wet atmospheres (wet air and wet 5% H_2) are much higher than those under dry atmospheres (dry air and dry H_2). The electrical transport activation energies showed the smallest value under dry 5% H_2 (i.e., 0.38 eV) and the largest value under dry air (i.e., 0.77 eV). While under wet atmospheres, the oxygen partial pressure did not affect the transport activation energies markedly. The activation energies under wet air and wet 5% H_2 are almost equal within the error range (0.51 eV vs. 0.48 eV). Besides, as the same as most proton conductivity under wet reducing atmosphere, the activation energies showed relatively smaller values in the higher temperature range (500°C-750°C) than at lower temperatures (300°C-500°C). Furthermore, the CS-20 BZY20 pellets' total conductivities under wet atmospheres are among the representative BZY20 pellets' highest region [48–53].

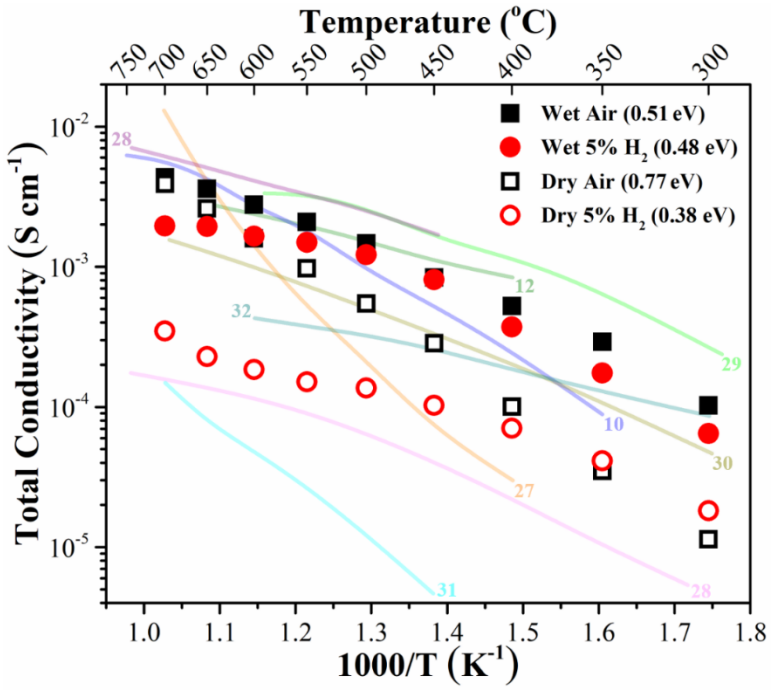


Figure 4.23. The temperature dependence of total conductivity under different atmospheres for CS-20, with comparing with representative BZY20 under wet atmospheres.

The study for the BZY20 pellets sintered at moderate temperature (i.e., 1500°C) indicated that the pretreatment of green pellets by cold sintering at 180°C with 20wt% water could result in fully densified phase pure BZY20 pellets. The cold sintering pretreatment could increase the barium carbonate amount inside the green pellet and the cold-sintered green pellet's relative density as described above. Therefore, we can ascribe the improved sinter ability of the BZY20 pellets to these effects.

The total conductivities for the CS-20 BZY20 pellets under wet air and wet 5% H_2 both are much higher than the respective dry atmospheres (dry air and dry 5% H_2). The significantly higher

electrical conductivities caused by water introduction come from the dominant proton conductivity in wet atmospheres, which is the same as other proton conducting oxides. The electrical transport activation energies of ~0.5 eV is consistent with proton conduction in perovskite-type oxides (e.g., BZY20). The lower increasing rate (lower activation energy) at the high-temperature range (500-750^{o}C) for the BZY20 under wet 5% H_2 results from the decrease in proton concentration and a minor increase in proton mobility, which is consistent with most of the other proton conducting oxides too [54–56]. When the atmospheres turn into dry atmospheres (dry air and dry 5% H_2), the electrical conductivities are much lower than those achieved under wet atmospheres. The high electrical transport activation energy of 0.77 eV under dry air is attributed to the lack of hydrogen or water in a dry air atmosphere. Thus, it is not surprised that the contribution of proton conductivity to the total conductivity is negligible. The lowest conductivity was observed with the test under dry 5% H_2. The lower concentration of protons in the BZY20 pellets due to the lack of water and the low oxygen partial pressure were hypothesized to result in a lower total conductivity. When we consider the activation energy, under dry 5% H_2 BZY20 shows the lowest value, even lower than the value observed under wet 5% H_2. The potential mixed ionic conduction (concomitant H^+ and O^{2-} transport) under a wet reducing atmosphere may cause the observed increased activation energy. Further studies aimed at understanding the conduction properties of the phase-pure and fully densified BZY20 are ongoing.

4.2.5 Initial study on catalyst addition strategies

In this section, we mainly focus on the catalyst's addition and the characterization of their influence on the morphology and performance of perovskite materials (ABO_3, or $BaZrO_3$ based). Two method were applied to add catalyst into the precursor powders.

i) Precursors with catalysts by modified Pechini method

The modified Pechini method is based on citric-EDTA acid complexing sol-gel method, which could obtain the atomic-level dispersion of precursors for the synthesis of the powders with smaller particles and higher purity. An additional 5 mol.% Ni, Cu or Pd nitrates were added into the BZY20 preparation recipe, followed by calcination at 900^{o}C for 10h to prepare the BZY20 powders with NiO, CuO or PdO.

ii) Precursors with catalysts by ball milling method

In this process, $BaCO_3$, ZrO_2, and Y_2O_3 in stoichiometric ratio were added into polyvinyl bottle with yttria-stabilized zirconia (YSZ) beans in isopropanol for 48h ball milling. Catalysts were added via an additional 5 mol.% NiO, CuO or PdO added into the suspension, following with air drying in oven at 90^{o}C for 24h.

Figure 4.24 shows the SEM images of BZY20 pellets obtained by conventional sintering process. Nano scale catalyst distributed uniformly in the porous structure. After reducing under 5 vol.% H_2

(balanced with Ar) at 650 ºC for 24 h, nanoscale catalysts were successfully loaded onto grain surface and in the grain boundaries for each sample added with Ni, Cu and Pd precursors.

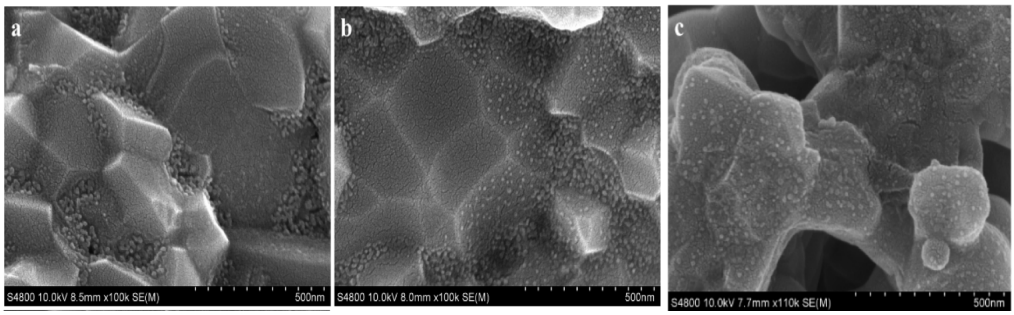


Figure 4.24. SEM images for cross-section of reduced BZY20 samples fabricated by conventional sintering process with (a) Ni, (b) Cu and (c) Pd catalyst, respectively.

Figure 4.25 presents the comparison of proton conductivity between BZY20 pellets with different catalysts. The conductivity changes gradually resulting in a continuous decrease of the thermal dependence. Pd catalyst shows high activity in high temperature range and has good dependent with temperature, while the conductivity of Cu sample is almost independent of temperature. When the intercept at highest frequency was used to calculate the proton conductivity, the bare and Pd sample have highest proton conductivity, whereas Ni sample has lowest proton conductivity. Because bare and Pd sample has highest porosity, this result implied porosity plays an important role in determining the proton conductivity which has been recognized in simple oxides (e.g., TiO_2, YSZ). In humidified atmosphere, water starts to absorb chemically on the oxide surfaces, which dissociation then results in hydroxyl groups,[57] which enhanced proton conductivity. Ni sample has lowest conductivity, which can be related to the big Ni particles due to cold pressing process. Further research will be conducted to optimize the fabrication method of homogenous catalyst particles.

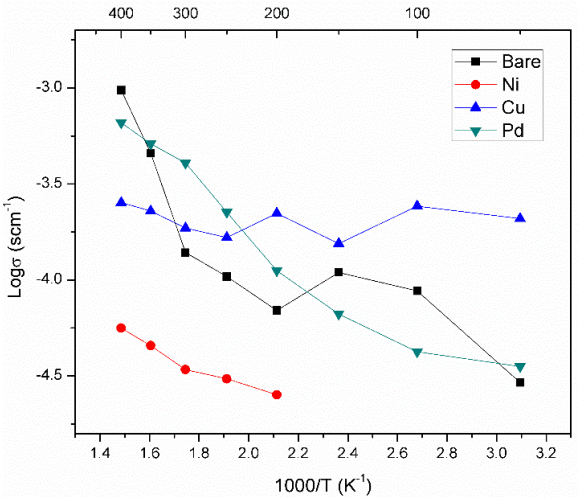


Figure 4.25. Comparison of proton conductivity for bare BZY20 and BZY20 with different catalysts.

4.2.6 PROCESS LEVEL CHARACTERIZATION PARAMETERS: SURFACE EXCHANGE AND DIFFUSION COEFFICIENTS

This sectiion provides information regarding the fundamental materials properties to be used in the modeling effort and documents completion of process level characterization. These studies include adsorption capacity of nanostructured TiO_2, BZY20 and BCZYYb (with and without catalysts) as function of grain size and porosity, the evaluation of different techniques such as Electrical Conductivity Relaxation (ECR) and in-situ Raman studies to obtain surface exchange coefficient k and diffusion coefficient D as a function of temperature. This data has been provided data to SRNL partners for use in modeling effort and process level economic analysis.

The materials system and techniques used to measure surface exchange coefficient *k* and diffusion coefficient *D* are listed in Table 4.2. The capacity was determined by TGA. At lower temperature (<300 °C), *k* and *D* can be determined by Raman and conductivity measurements (through Nernst-Einstein equation). At higher temperature (>300 °C), Electrical Conductivity Relaxation (ECR) fitting was used to extract *k* and *D*.

Table 4.2. Materials system and key parameters for modeling.

Materials	Sintering	Catalysts	Capacity	Surface exchange coefficient (*k*)		Diffusion coefficient (D)	
				< 300 °C	> 300 °C	< 300 °C	> 300 °C
TiO_2	Traditional	Fe	0.7%	Raman	TGA	Nernst-Einstein	Doping
BZY20	Traditional Cold sintering	Cu, Ni, Pd	> 0.07% [1]	Raman/TGA	ECR	Nernst-Einstein	ECR
BCZYYb	Traditional, Cold sintering	Cu, Ni, Pd	NA	Raman/TGA	ECR	Nernst-Einstein	ECR

Surface exchange coefficient k and Diffusion coefficient D

Low temperature (< 300 °C)

In-situ Raman spectroscopy was applied to probe the surface exchange reaction between H_2O and D_2O in the low temperature *(< 300 °C)* regime. Figure 4.26 shows the dependence of Raman spectra intensity with time after switching the atmosphere from Ar/H_2O to Ar/D_2O at 25 °C. There is vibrating bond changing from OH to OD at 25 °C, indicating a Grotthuss mechanism of the proton transport in nanostructured TiO_2 membrane. The decrease in the integrated intensity of OH vibration follows a straight line in the semi-logarithmic plot, and it is possible to define a first-order rate constant, $k_{H/D}$ of 8.19 x 10^{-5} s^{-1}. The H/D exchange rate constant is a slightly lower than the value observed in polymeric structures (α-Methylene[58]).

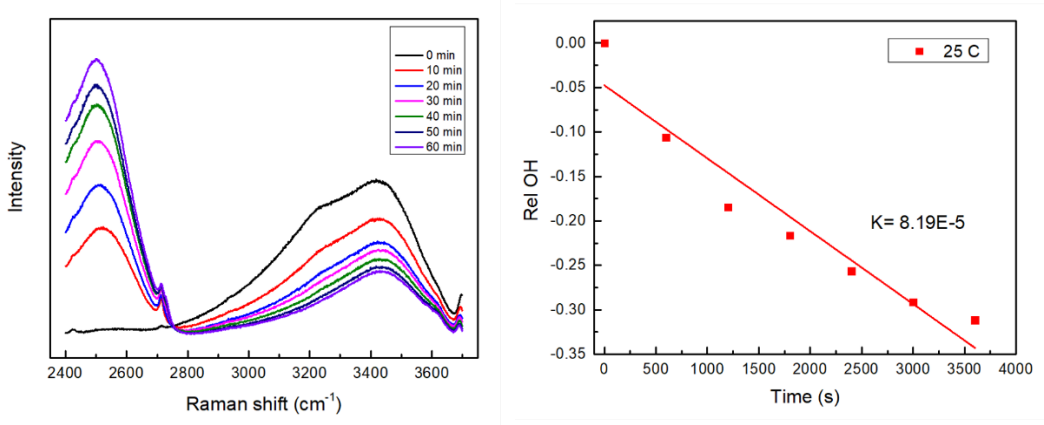


Figure 4.26. Time-dependent Raman spectra after switching the atmosphere from H_2O-air to D_2O-air at 25 °C and logarithm of the integrated relative Raman OH vibration intensity in nanostructured TiO_2 membrane as a function of time of exposure to H_2O and D_2O, respectively.

Electrochemical impedance spectra (EIS) were applied to measure the proton conductivity under air/H_2O and air/D_2O, as shown in Figure 4.27. Like the porous TiO_2 membranes reported before, the conductivity increased as the temperature decreased from 250 °C to room temperature in all three samples. Also, the conductivity was found to be strongly dependent on the grain size. The membrane with the smallest grain size showed the highest conductivity, which resulted from increased absorbed water in the interface. The diffusion coefficient can be calculated by applying the Nernst-Einstein equation with results displayed in Table 2.

$$D_i = \sigma_i \frac{KT}{C_i Z_i^2 e^2}$$

Compared to the data reported in the literature[59], the effective diffusion coefficients of $Ba_{0.5}Sr_{0.5}Fe_{0.8}Zn_{0.2}O_{3-d}$ are ranging from 1.4 to 29 $\times 10^{-7}$ cm^2 s^{-1} (350 to 600 °C), which is very close to that of TiO_2 sintered at 650 °C.

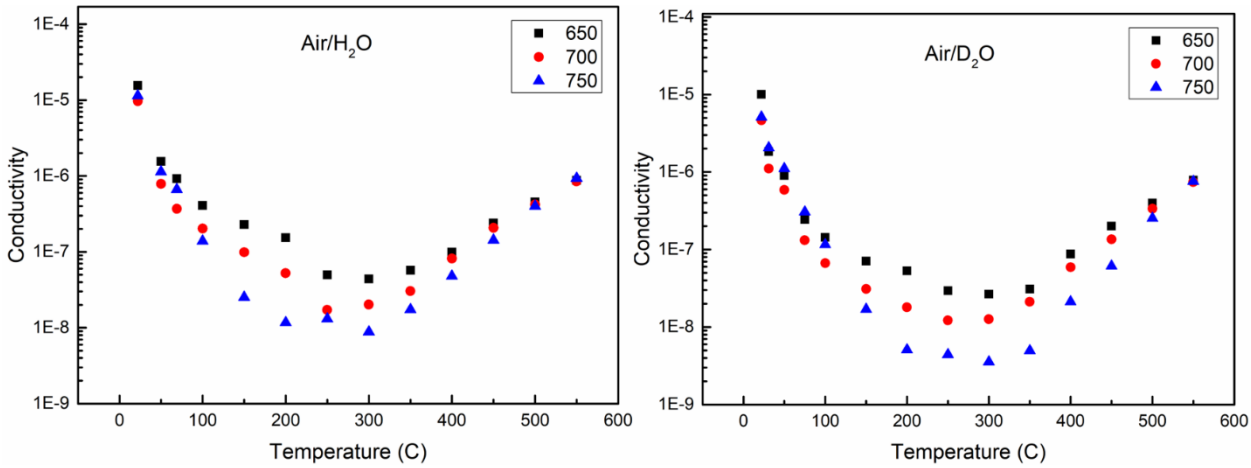


Figure 4.27. Total conductivity of nanostructured TiO_2 membrane by SPS method in air/H_2O and air/D_2O

High temperature (>300 °C)

In the high temperature range ECR was used to obtain *k* and *D*. Because TiO_2 is nonconductive, we will use Nd-doped TiO_2 for subsequent ECR experiment.

Table 4.3. Total conductivity (σ) and diffusion coefficient (D) of nanostructured TiO_2 by SPS method under air/H_2O and air/D_2O

	650 °C	650 °C	650 °C	650 °C	700 °C	700 °C	700 °C	700 °C	750 °C	750°C	750 °C	750 °C
T(K)	σ (H) (S/cm)	σ (D) (S/cm)	D (H) (cm^2/s)	D (D) (cm^2/s)	σ (H) (S/cm)	σ(D) (S/cm)	D (H) (cm^2/s)	D (D) (cm^2/s)	σ (H) (S/cm)	σ (D) (S/cm)	D (H) (cm^2/s)	D (D) (cm^2/s)
823	9.21E-07	3.26E-10	4.08E-10	7.40E-07	8.22E-07	7.40E-07	3.65E-10	3.28E-10	7.35E-07	7.56E-07	3.26E-10	3.35E-10
773	4.56E-07	1.11E-10	1.90E-10	3.37E-07	4.14E-07	3.37E-07	1.72E-10	1.41E-10	2.71E-07	2.54E-07	1.13E-10	1.06E-10
723	2.53E-07	2.89E-11	9.86E-11	1.36E-07	1.83E-07	1.36E-07	7.15E-11	5.30E-11	7.42E-08	6.13E-08	2.89E-11	2.39E-11
673	9.99E-08	9.19E-12	3.62E-11	5.92E-08	7.70E-08	5.92E-08	2.79E-11	2.15E-11	2.53E-08	2.12E-08	9.19E-12	7.70E-12
623	5.89E-08	3.51E-12	1.98E-11	2.12E-08	2.85E-08	2.12E-08	9.56E-12	7.12E-12	1.04E-08	4.96E-09	3.51E-12	1.67E-12

573	3.76E-08	1.67E-12	1.16E-11	1.26E-08	1.86E-08	1.26E-08	5.74E-12	3.90E-12	5.42E-09	3.55E-09	1.67E-12	1.10E-12
523	4.27E-08	1.27E-12	1.20E-11	1.22E-08	1.91E-08	1.22E-08	5.40E-12	3.45E-12	4.51E-09	4.42E-09	1.27E-12	1.25E-12
473	9.51E-08	1.57E-12	2.43E-11	1.80E-08	3.62E-08	1.80E-08	9.22E-12	4.58E-12	6.16E-09	5.11E-09	1.57E-12	1.30E-12
423	1.92E-07	5.63E-12	4.37E-11	3.09E-08	8.00E-08	3.09E-08	1.82E-11	7.05E-12	2.47E-08	1.70E-08	5.63E-12	3.87E-12
373	3.81E-07	3.11E-11	7.65E-11	6.70E-08	1.32E-07	6.70E-08	2.65E-11	1.35E-11	1.55E-07	1.17E-07	3.11E-11	2.35E-11
348	8.12E-07	9.23E-11	1.52E-10	1.32E-07	2.70E-07	1.32E-07	5.06E-11	2.47E-11	4.92E-07	3.05E-07	9.23E-11	5.72E-11
323	1.97E-06	2.91E-10	3.44E-10	5.89E-07	9.23E-07	5.89E-07	1.61E-10	1.03E-10	1.67E-06	1.11E-06	2.91E-10	1.93E-10
304	3.64E-06	4.70E-10	5.97E-10	1.11E-06	1.79E-06	1.11E-06	2.93E-10	1.82E-10	2.87E-06	2.06E-06	4.70E-10	3.37E-10
295	1.90E-05	1.22E-09	3.03E-9	4.63E-06	7.06E-06	4.63E-06	1.12E-9	7.37E-10	7.64E-06	5.11E-06	1.22E-9	8.12E-10

Process level property characterization will be presented for optimized materials with varying catalyst additions. To obtain dense TiO_2 membrane with different catalysts, NiO, Fe_2O_3 and CuO were mixed with nano scale TiO_2 powder, respectively, followed by densification with SPS method at 700 °C. Improved conductivity was observed for the sample with catalyst at low temperatures. At room temperature, the proton conductivity increased by a factor of 5.5, 1.7 and 2.9 with NiO, Fe_2O_3 and CuO as catalyst, respectively (Figure 4.28). Similarly, the proton diffusion coefficient was calculated by the Nernst- Einstein equation.

It is reported that the diffusion coefficient of OH in the bulk of TiO_2 was about 0.11 $Å^2\ ps^{-1}$ ($1.1 \times 10^{-5}\ cm^2\ s^{-1}$).[60] The diffusion coefficient increased from $1.89 \times 10^{-9}\ cm^2\ s^{-1}$ to $1.0 \times 10^{-8}\ cm^2\ s^{-1}$ and $5.3 \times 10^{-9}\ cm^2\ s^{-1}$, with NiO and Fe_2O_3 as catalyst, respectively. Obviously, the diffusion coefficient is still lower than bulk materials. However, the conductivity is higher than the value in the literature[61] because of its nano-structure.

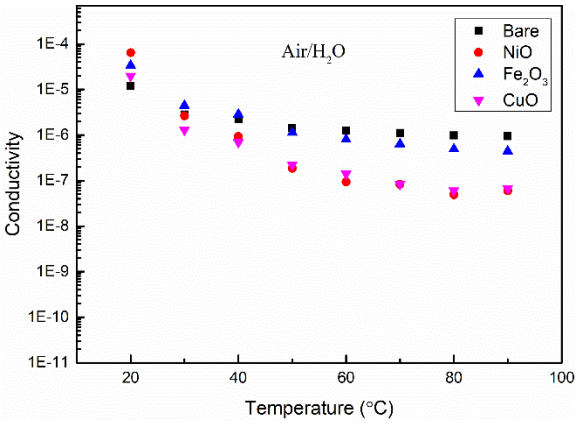


Figure 4.28. Total conductivity of dense TiO_2 by SPS method with different catalyst (5 wt% oxides) in humified air.

Table 4.4. Total conductivity and diffusion coefficient of nanostructured TiO_2 with different oxides by SPS method under air/H_2O

	Bare	Bare	NiO	NiO	Fe_2O_3	Fe_2O_3	CuO	CuO
T(K)	Conductivity (S/cm)	Diffusion coefficient (cm^2/s)	Conductivity (S/cm)	Diffusion coefficient (cm^2/s)	Conductivity (S/cm)	Diffusion coefficient (cm^2/s)	Conductivity (S/cm)	Diffusion coefficient (cm^2/s)
363	9.37E-07	1.83E-10	6.00E-08	1.17E-11	4.46E-07	8.72E-11	6.65E-08	1.30E-11
353	9.76E-07	1.86E-10	4.90E-08	9.32E-12	4.94E-07	9.40E-11	5.98E-08	1.14E-11
343	1.11E-06	2.06E-10	8.33E-08	1.54E-11	6.38E-07	1.18E-10	8.34E-08	1.54E-11
333	1.26E-06	2.25E-10	9.28E-08	1.67E-11	8.04E-07	1.44E-10	1.41E-07	2.53E-11
323	1.41E-06	2.46E-10	1.86E-07	3.25E-11	1.13E-06	1.98E-10	2.21E-07	3.85E-11
313	2.21E-06	3.73E-10	9.28E-07	1.57E-10	2.87E-06	4.84E-10	6.93E-07	1.17E-10
303	2.84E-06	4.63E-10	2.63E-06	4.29E-10	4.45E-06	7.28E-10	1.29E-06	2.10E-10
293	1.17E-05	1.85E-9	6.44E-05	1.017E-8	3.38E-05	5.33E-9	1.99E-05	3.14E-9

Capacity

Surface capacity can be determined by TGA and bulk capacity can be determined from oxygen stoichiometry. The results are shown in Table 4.5.

Table 4.5. Surface and bulk capacity of BZY20.

	Surface capacity	Bulk capacity
TGA	>0.07%	/
BET	TGA - Stoichiometry	/
Stoichiometry	/	0.65%

Surface exchange coefficient k Diffusion coefficient D

Electrochemical impedance spectra (EIS) were applied to measure the proton conductivity under 3% H_2O wetted air at temperature lower than 300 °C (Figure 4.29). The EIS can be fitted using equivalent circuit to separate the bulk resistance and grain boundary resistance at temperature range lower than 300 °C. High frequency range (R2) can be ascribed to bulk resistance and R3 can be ascribed to grain boundary resistance.

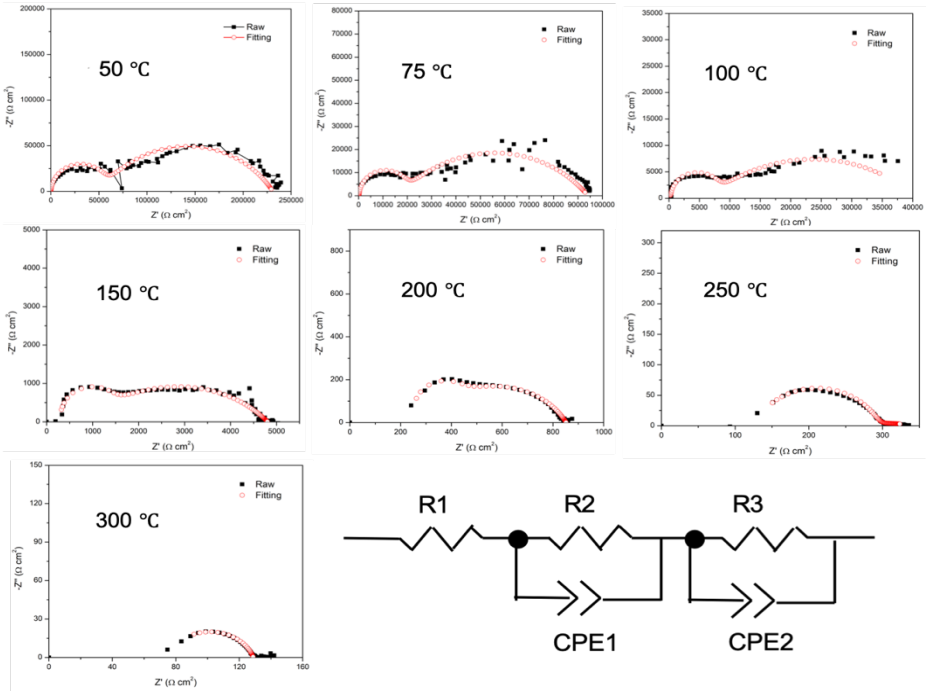


Figure 4.29. EIS data of cold-sintered BZY20 measured under 3% wet air.

Through use of the Nernst-Einstein equation, the diffusion coefficient can be calculated as displayed in Table 4.6.

$$D = \frac{\sigma RT}{F^2 C_i}$$

Table 4.6. Diffusion coefficient *D* obtained using Nernst-Einstein equation.

Temperature (°C)	50	75	100	150	200	250	300
D (cm^2/s)	$8.58*10^{-11}$	$8.42*10^{-11}$	$5.63*10^{-10}$	$5.65*10^{-9}$	$4.64*10^{-8}$	$1.41*10^{-7}$	$1.35*10^{-7}$
D_{Bulk} (cm^2/s)	$3.69*10^{-10}$	$1.21*10^{-10}$	$3.46*10^{-9}$	$3.40*10^{-8}$	$2.91*10^{-7}$	$2.00*10^{-7}$	$7.65*10^{-7}$
D_{GB} (cm^2/s)	$9.45*10^{-11}$	$2.19*10^{-10}$	$4.92*10^{-10}$	$4.37*10^{-9}$	$3.19*10^{-8}$	$2.48*10^{-7}$	$7.85*10^{-8}$

4.2.7 Transport Model and Process Based Economic Analysis

The state of art technology for tritium separation is the combined electrolysis and catalytic exchange (CECE) process combines a liquid phase catalytic exchange (liquid phase catalytic exchange) column with an electrolysis cell to split hydrogen from water. A portion of the gaseous hydrogen from the electrolysis cell is drawn off, while the remainder is refluxed to the LPCE. With this internal recycle, the CECE process provides a vapor product stream concentrated in tritium. A zeolite membrane separation process utilizes Linde Type A zeolite membranes. The tritiated water evaporates through the membrane and is condensed and collected. The condensed permeate is then sent through more stages in series until the desired purity is achieved. The separation factor for these membranes is about 2, and a feasible process may require over 70 stages.

The process described in this milestone, based on a novel proton conducting material, would operate as an isotope exchange bed, shown on Figure 4.30. Similar to an adsorption bed, the tritiated feedwater would be passed through a bed of proton conducting material. The tritium in the feedwater exchanges with the hydrogen in the proton conducting material, removing the tritium from the liquid phase. Clean water is output during this phase of the operation. Once the material in the bed is isotopically saturated, the bed is drained of water, and steam is used to regenerate the bed. Superheated steam is passed in the reverse direction of the feedwater. The steam simultaneously heats the bed and removes tritium from the bed material. Once the bed material is cleaned, the bed is cooled and returned to service, able to clean more tritiated feedwater.

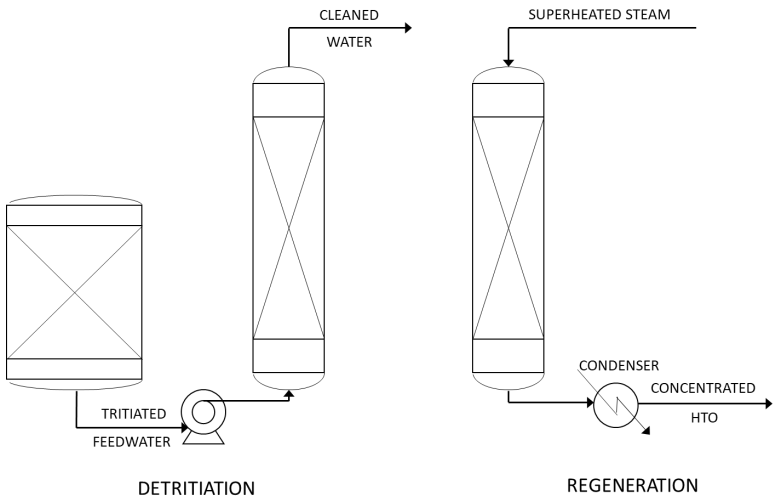


Figure 4.30. Single-stage proton conducting isotope exchange process

Basic economic analyses have been based on the energy required to drive the separation processes used to detritify water. The CECE process is estimated to cost $1.7/L to operate[4]. The Linde Type A zeolite membrane process is estimated to cost $0.27/L[3]. A process based on the novel proton conducting material described in this work could cost $0.19/L to operate.

Isotopic Separation Data

Initial measurements of the isotopic separation factors were obtained using in-situ Raman spectroscopy in nanocrystalline BaCe0.7Zr0.1Y0.1Yb0.1O3-δ (BCZYYb). Modified Pechini method was used to synthesis nano BCZYYb powder, and dry press method was applied to fabricate the nanostructure membrane without high temperature sintering for isotope exchange experiments. The isotope exchange measurements were performed in a water-cooled hot stage (Linkham, TS1500) by flowing Ar through bubblers with mixed D_2O and H_2O at different temperatures to control the water vapor content. The isotopic ratios in the solid in equilibrium with the given liquid phase ratios are shown in Table 4.74.7.

Table 4.7. Measured isotopic ratios by in-situ Raman spectroscopy from 25 to 300 ºC

Temperature (°C)	50:50 D:H	20:80 D:H
25	1:1.20	1:2.02
100	1:1.59	1:2.35
200	1:2.42	1:4.60
300	1:2.75	1:5.41

The isotopic ratios of Table 4.7 are converted into separation factors and shown in Figure 4.31, with y representing the mole fraction in the fluid phase and x the mole fraction in the solid phase. Although these initial separation factors are not constant with fluid phase composition, they show a consistent trend with temperature.

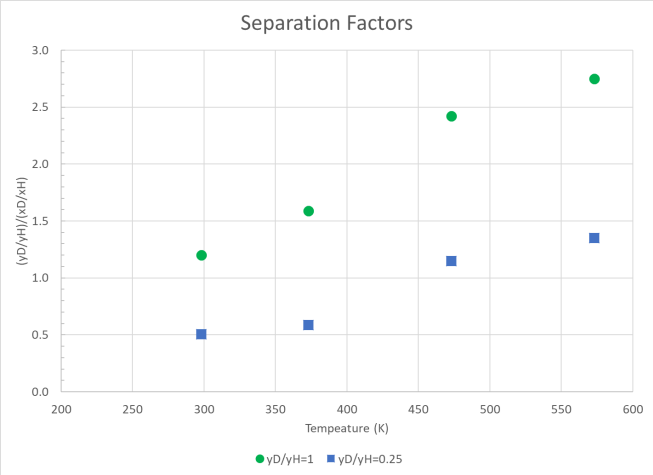


Figure 4.31. Measured separation ratios converted to separation factors from 25 to 300 ºC.

For the yD/yH = 0.25 case, the separation factor crosses unity. This behavior is ideal for separation processes. At 25 °C, the separation factor is 0.505, while it is 1.35 at 300 °C. Figure 4.32**Error! Reference source not found.** shows the equilibrium concentration profiles if these separation factors were constant at fluid phase compositions below 20:80 D: H. From the concentration profiles, a bed operating at separation factor below 1.0 will have a solid phase enriched in the heavier isotope, and one operating at a separation factor above 1.0 will have a lean solid phase.

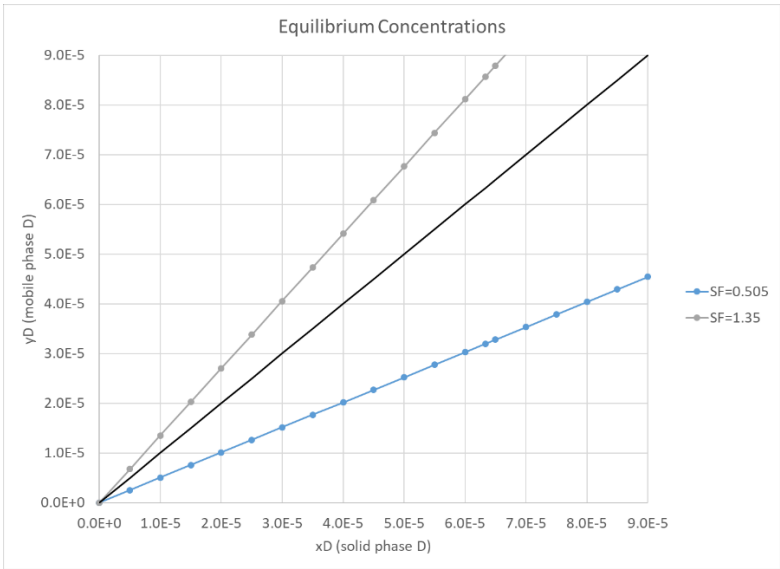


Figure 4.32. Equilibrium compositions for constant separation factors

In the case of the measured separation factors above, the room temperature separation factor is measured at 0.505, while at 300 °C it is measured to be 1.35. This presents a tremendous advantage if the bed is used at room temperature to remove tritium from the water feed, while it is regenerated with steam at 300 °C, as shown in Figure 4.33.

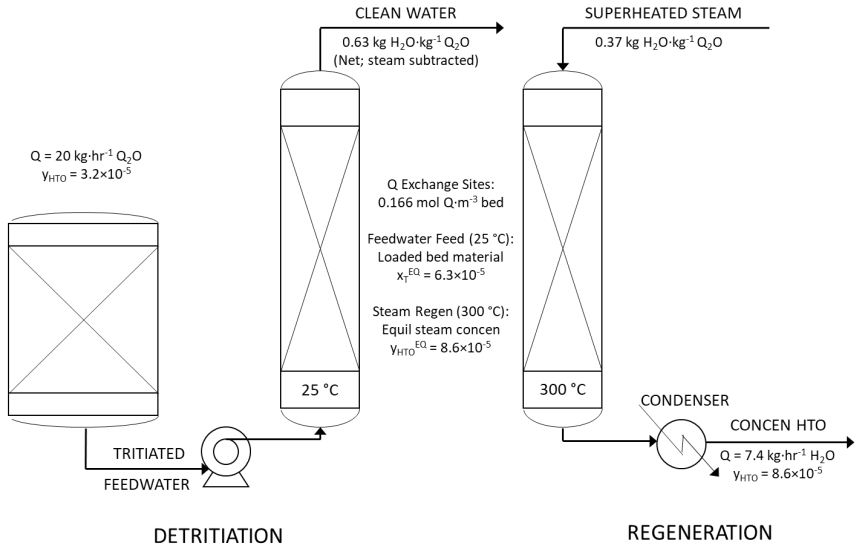


Figure 4.33. Bed operating modes for tritium separation and regeneration.

Preliminary Performance Evaluation

From the provided separation factors, the tritium cleanup will occur from liquid phase water at room temperature. The current data give a separation factor of 0.505 for a 20:80 T:D ratio at this temperature. Although the tritium concentration of the input stream is far lower, the value of 0.505 will be used until a better measurement of the separation factor is available.

Using the 5.638 g·cm^{-3} density, 0.7 wt% OH loading, and assuming a bed void fraction of 0.5, the concentration of active hydrogen exchange sites is 1.16×10^{-3} mol H·m^{-3} bed. For comparison, there are 0.0553 mol H·cm^{-3} bed in the liquid water phase, using 0.997 g·cm^{-3} for water's liquid density.

For a tritiated water feed of 3.2×10^{-5} mol fraction HTO, there is 1.77×10^{-6} mol T·cm^{-3} Q_2O. At the 0.505 separation factor, the bed tritium concentration in equilibrium with this feed is 6.34×10^{-5} mol fraction T. This equates to 7.35×10^{-8} mol T·cm^{-3} bed. From these calculations, each cm^3 of clean bed could remove the tritium from 4.15×10^{-2} cm^3 Q_2O at 25 °C.

Bed regeneration is taken to occur at 300 °C to maximize the separation factor at 1.35. To minimize volume of the concentrated tritiated water output, we assume the steam heating the bed is kept separate from the bed material and the steam being used to regenerate the bed. At the adsorbed concentration of 6.34×10^{-5} mol fraction T, the equilibrium vapor concentration is 8.57×10^{-5} mol

fraction HTO. To remove 7.35×10^{-8} mol T·cm^{-3} bed, it would take 8.58×10^{-4} mol H_2O·cm^{-3} bed at 300 °C. This corresponds to using 1.55×10^{-2} cm^3 H_2O·cm^{-3} bed for regeneration.

Neglecting the non-equilibrium state within the concentration profile region of the bed, a tritiated stream at 3.2×10^{-5} mol fraction HTO can be concentrated to 8.57×10^{-5} mol fraction HTO, providing a net 0.627 cm^3 clean H_2O per cm^3 of tritiated water feed.

Table 4.8. Adsorbent capacity and required steam regeneration

Quantity	Value	Units
Adsorbent capacity		
OH loading	0.7	wt% OH
Adsorbent density	5.638	g·cm^{-3}
Porosity	0.5	
Q sites	1.16×10^{-3}	mol·cm^{-3} bed
Feed treatment (room temperature)		
Feed composition	3.20×10^{-5}	y_{HTO}
Feed density	0.997	g·cm^{-3}
T in feed	1.77×10^{-6}	mol T·cm^{-3} Q_2O
Separation factor	0.505	
Equilibrium Q sites	6.34×10^{-5}	x_T
Equilibrium T in bed	7.35×10^{-8}	mol·cm^{-3} bed
Feed treated	4.15×10^{-2}	g Q_2O·cm^{-3} bed
Bed regeneration (steam regeneration)		
Separation factor	1.35	
Equilibrium vapor	8.57×10^{-5}	y_{HTO}
Required steam	1.55×10^{-2}	g H_2O·cm^{-3} bed

Economic Evaluation

The processing rate for this analysis is set to 20 kg·hr^{-1}. At this rate, it is possible to design a bed to handle two hours' worth of feed, 40 kg. With a 30% design margin, the necessary bed volume

is 1.26 m^3 for an adsorbate with 0.5 bed porosity. Using a diameter of 0.407 m (16 in), we have bed 9.69 m (32 ft) long with an L/D ratio of over 23. Separating the bed into multiple sections would facilitate either a rotating regeneration scheme or allow simultaneous regeneration of multiple bed sections.

Because of the quantity of heating and cooling needed for bed regenerations, we assume the process design will incorporate heat integration to reduce utility costs as much as possible. Here, we assume a minimum temperature approach of 10 °C, assuming that all heating and cooling except for the final 10 °C can be handled through heat recovery integration.

0.73 GJ would be needed to heat this amount of adsorbate from 25 °C to 300 °C, assuming 0.75 $kJ \cdot kg^{-1} \cdot K^{-1}$ heat capacity. To heat the bed vessel, 0.12 GJ of heat would be needed if we assume a standard steel tube having 0.5 $kJ \cdot kg^{-1} \cdot K^{-1}$ heat capacity. Combined, we would need to provide 0.86 GJ to heat the bed for regeneration. Without heat recovery, we would need to supply 4.6 tonne of steam and 0.86 GJ of cooling. But only having to heat or cool the last 10 °C means we only need to supply 0.65 tonne of steam or 0.031 GJ of cooling. In addition to that heating and cooling requirement, 0.021 tonne of steam is needed for the actual regeneration of tritium from the bed. As a broad assumption, we use 20 $kWh \cdot day^{-1}$ as an estimated demand for pumping, vacuum, and related process power requirements.

Assuming \$0.1·kWh^{-1} energy cost and \$8.11·$tonne^{-1}$ steam cost, along with 50% cooling losses and 70% steam efficiency, the yearly operating cost is about \$33K, as shown below.

Table 4.9. Bed sizing and yearly operating cost estimate

Quantity	Value	Unit
Required processing rate	20	$kg \cdot hr^{-1}$
Bed sizing		
2-hour processing quantity	40	kg Q_2O
Design margin	30%	
Adsorbate volume	1.26	m^3
Bed diameter	0.407	m
Bed length (total)	9.69	m
Energy cost		
Year processing rate	175	tonne Q_2O
Cost of cooling	0.1	\$·$kWhr^{-1}$

Required cooling	38,963	$kWh \cdot yr^{-1}$
Cooling efficiency	50%	
Cooling cost	7,793	$\$ \cdot yr^{-1}$
Energy for pumps, vacuum, etc.	7,300	$kWh \cdot yr^{-1}$
Cost of pumps, vacuum, etc.	1,460	$\$ \cdot yr^{-1}$
Yearly energy cost	9,253	$\$ \cdot yr^{-1}$
Steam cost		
Natural gas cost	2.27	$\$ \cdot GJ^{-1}$
Natural gas efficiency	85%	
Steam cost (330 °C, 1 atm)	8.11	$\$ \cdot tonne^{-1}$
Steam usage efficiency	70%	
Mass of steam for regeneration	93.5	$tonne \cdot yr^{-1}$
Mass of steam for bed heating	2,827	$tonne \cdot yr^{-1}$
Steam cost	23,683	$\$ \cdot yr^{-1}$
Total yearly cost	32,936	$\$ \cdot yr^{-1}$

The use of proton conducting membrane materials as isotopically selective adsorption materials, have the potential to be an economically viable process for water detritiation. This preliminary evaluation estimates a system based on an adsorption/regeneration cycle utilizing a 1.26 m^3 bed would have annual operating costs about $33K to selectively remove tritium from 175 tonnes of low-tritiated water. In this configuration, the cost of detritation is approximately $0.19/L.

Future work is needed to validate economic viability and acquire data needed to construct a proof-of-concept system. Future work includes:

1) Accurate separation factors over the temperature and concentration ranges of interest.
2) Determination of separation factors with liquid phase feed (current experimental data determined with Ar gas feed containing water vapor).
3) Fabrication methods for the adsorbent particles.
4) Measurements of the adsorbent capacity, selectivity, specific heat, etc.
5) Durability of material to repeated changes in process conditions.

CONCLUSIONS

In this project, two categories of materials were explored including i) simple oxides (TiO_2), ii) perovskite phases based on zirconates ($BaZr_{0.8}Y_{0.2}O_{2.9}$). Nanostructured ceramic membranes were fabricated from the crystalline materials utilizing three principal methods: i) conventional sintering (including one and two step sintering processes), ii) spark plasma sintering and iii) cold sintering.

- We successfully fabricated TiO_2 membrane at 120℃ by cold sintering method, the relative density of the pellet is more than 70%, which is much higher than the pellet made by uniaxially pressure at same conditions.
- The increased conductivity of nanostructured TiO_2 membrane in the wet atmosphere and its polarization behavior confirm the existence of the proton conductivity in the nanoscale TiO_2 membrane at low temperatures (< 250 ºC). The difference of proton conductivity in H_2O and D_2O reveals the hopping mechanism of the proton conduction.
- In-situ Raman spectroscopy was used to directly identify the proton transport mechanism on the interface of nanostructured ceramic membranes. The observed isotope exchange reactions on the interface indicates a Grotthuss or "hopping" type mechanism of proton transport which is selective isotopes based on mass. In addition, the estimated surface concentration of protons in simple oxides is comparable to the calculated bulk content of protons for typical perovskite based protonic conductors indicating the potential for enhanced conduction
- Effects of sintering process and water amount on the morphology of $BaZr_{0.8}Y_{0.2}O_{3-\delta}$ were investigated. Uniform grain sizes and lower density were obtained by decreasing sintering temperature. Regarding the water amount, higher water concentration results in larger grain size and higher relative density. The optimized cold sintering conditions, including tailored porosity could provide options for nano-structure membranes of use in this project.
- Using an optimum amount 5 mol% Cu as catalyst, a BZY20 pellet with an average grain size around 120 nm and relative density of 97% was obtained.
- We demonstrate a cold sintering pretreatment of BZY20 helped to produce dense ceramics at a moderate temperature of 1500ºC. The as-fabricated BZY20 pellets showed a phase-pure perovskite structure, high relative density, and desired microstructure. Introducing the proper amount of $BaCO_3$ on the precursor particle surface and the high green density for the green pellets with homogenous microstructure achieved by cold sintering pretreatment were responsible for lowering the final sintering temperature.
- The preliminary evaluation estimates a system based on an adsorption/regeneration cycle utilizing a 1.26 m^3 bed would have annual operating costs about $33K to selectively remove tritium from 175 tonnes of low-tritiated water. In this configuration, the cost of detritation is approximately $0.19/L.

NEUP PUBLICATION AND PRESENTATION LIST [1–5]

[1] Y. Meng, J. Gao, Z. Zhao, J. Amoroso, J. Tong, K.S. Brinkman, Review: recent progress in low-temperature proton-conducting ceramics, J Mater Sci. 54 (2019) 9291–9312. https://doi.org/10.1007/s10853-019-03559-9.

[2] K.S. Brinkman, Y. Meng, J. Gao, Z. Zhao, J. Amoroso, Jianhua, (Invited) Recent Progress in Low-Temperature Proton Conducting Ceramics for Hydrogen Isotope Processing, in: ECS, 2019. https://ecs.confex.com/ecs/236/meetingapp.cgi/Paper/125982 (accessed July 23, 2020).

[3] J. Gao, Y. Meng, A. Benton, J. He, L.G. Jacobsohn, J. Tong, K.S. Brinkman, Insights into the Proton Transport Mechanism in TiO2 Simple Oxides by In Situ Raman Spectroscopy, ACS Appl. Mater. Interfaces. (2020). https://doi.org/10.1021/acsami.0c08120.

[4] Z. Zhao, J. Gao, Y. Meng, K.S. Brinkman, J. Tong, Moderate temperature sintering of BaZr0.8Y0.2O3-δ protonic ceramics by A novel cold sintering pretreatment, Ceramics International. (2021) S0272884220338736. https://doi.org/10.1016/j.ceramint.2020.12.257.

[5] J. Gao, Y. Meng, J. Duffy, K. Brinkman, " Low-Temperature Protonic Ceramic Fuel Cells through Interfacial Engineering of Nanocrystalline BaCe0.7Zr0.1Y0.1Yb0.1O3δ Electrolytes" Advanced Energy and Sustainability Research, 2021, 2100098, DOI: 10.1002/aesr.202100098

REFERENCES

[1] K.D. Kreuer, Proton-Conducting Oxides, Annual Review of Materials Research. 33 (2003) 333–359. https://doi.org/10.1146/annurev.matsci.33.022802.091825.

[2] H. Iwahara, T. Esaka, H. Uchida, N. Maeda, Proton conduction in sintered oxides and its application to steam electrolysis for hydrogen production, Solid State Ionics. 3–4 (1981) 359–363. https://doi.org/10.1016/0167-2738(81)90113-2.

[3] T. Norby, Solid-state protonic conductors: principles, properties, progress and prospects, Solid State Ionics. 125 (1999) 1–11. https://doi.org/10.1016/S0167-2738(99)00152-6.

[4] S.M. Haile, D.L. West, J. Campbell, The role of microstructure and processing on the proton conducting properties of gadolinium-doped barium cerate, Journal of Materials Research. 13 (1998) 1576–1595. https://doi.org/10.1557/JMR.1998.0219.

[5] M.T. Caldes, K.V. Kravchyk, M. Benamira, N. Besnard, V. Gunes, O. Bohnke, O. Joubert, Metallic Nanoparticles and Proton Conductivity: Improving Proton Conductivity of BaCe0.9Y0.1O3−δ Using a Catalytic Approach, Chem. Mater. 24 (2012) 4641–4646. https://doi.org/10.1021/cm301685x.

[6] M. van den Bossche, S. McIntosh, Pulse Reactor Studies to Assess the Potential of La0.75Sr0.25Cr0.5Mn0.4X0.1O3-δ (X = Co, Fe, Mn, Ni, V) as Direct Hydrocarbon Solid Oxide Fuel Cell Anodes, Chem. Mater. 22 (2010) 5856–5865. https://doi.org/10.1021/cm101567v.

[7] D.-K. Lim, C.-J. Park, M.-B. Choi, C.-N. Park, S.-J. Song, Partial conductivities of mixed conducting BaCe{sub 0.65}Zr{sub 0.2}Y{sub 0.15}O{sub 3-{delta}}, International Journal of Hydrogen Energy. 35 (2010). https://doi.org/10.1016/J.IJHYDENE.2010.07.122.
[8] D.-K. Lim, S.-Y. Jeon, B. Singh, J.-Y. Park, S.-J. Song, Surface exchange kinetics and chemical diffusivities of BaZr0.2Ce0.65Y0.15O3−δ by electrical conductivity relaxation, Journal of Alloys and Compounds. 610 (2014) 301–307. https://doi.org/10.1016/j.jallcom.2014.05.028.
[9] G. Gregori, M. Shirpour, J. Maier, Proton Conduction in Dense and Porous Nanocrystalline Ceria Thin Films, Advanced Functional Materials. 23 (2013) 5861–5867. https://doi.org/10.1002/adfm.201300527.
[10] F. Maglia, I.G. Tredici, G. Spinolo, U. Anselmi-Tamburini, Low temperature proton conduction in bulk nanometric TiO2 prepared by high-pressure field assisted sintering, Journal of Materials Research. 27 (2012) 1975–1981. https://doi.org/10.1557/jmr.2012.158.
[11] X. Wang, Y. Ma, S. Li, A.-H. Kashyout, B. Zhu, M. Muhammed, Ceria-based nanocomposite with simultaneous proton and oxygen ion conductivity for low-temperature solid oxide fuel cells, Journal of Power Sources. 196 (2011) 2754–2758. https://doi.org/10.1016/j.jpowsour.2010.11.033.
[12] D. Pergolesi, E. Fabbri, A. D'Epifanio, E. Di Bartolomeo, A. Tebano, S. Sanna, S. Licoccia, G. Balestrino, E. Traversa, High proton conduction in grain-boundary-free yttrium-doped barium zirconate films grown by pulsed laser deposition, Nature Materials. 9 (2010) 846–852. https://doi.org/10.1038/nmat2837.
[13] L. Malavasi, C.A.J. Fisher, M.S. Islam, Oxide-ion and proton conducting electrolyte materials for clean energy applications: structural and mechanistic features, Chemical Society Reviews. 39 (2010) 4370. https://doi.org/10.1039/b915141a.
[14] M. Yamada, M. Wei, I. Honma, H. Zhou, One-dimensional proton conductor under high vapor pressure condition employing titanate nanotube, Electrochemistry Communications. 8 (2006) 1549–1552. https://doi.org/10.1016/j.elecom.2006.07.020.
[15] D. Clark, J. Tong, A. Morrissey, A. Almansoori, I. Reimanis, R. O'Hayre, Anomalous low-temperature proton conductivity enhancement in a novel protonic nanocomposite, Phys. Chem. Chem. Phys. 16 (2014) 5076–5080. https://doi.org/10.1039/C4CP00468J.
[16] C.P. Cameron, R. Raj, Grain-Growth Transition During Sintering of Colloidally Prepared Alumina Powder Compacts, Journal of the American Ceramic Society. 71 (1988) 1031–1035. https://doi.org/10.1111/j.1151-2916.1988.tb05787.x.
[17] R.J. Brook, Controlled Grain Growth, in: Treatise on Materials Science & Technology, Elsevier, 1976: pp. 331–364. https://doi.org/10.1016/B978-0-12-341809-8.50024-3.
[18] R.H.R. Castro, K. van Benthem, eds., Sintering: mechanisms of convention nanodensification and field assisted processes, Springer, Berlin ; New York, 2013.
[19] I.-W. Chen, X.-H. Wang, Sintering dense nanocrystalline cramics withourt final-stage grain growth, Nature. 404 (2000) 168–171.
[20] X.-H. Wang, P.-L. Chen, I.-W. Chen, Two-Step Sintering of Ceramics with Constant Grain-Size, I. Y2O3, Journal of the American Ceramic Society. 89 (2006) 431–437. https://doi.org/10.1111/j.1551-2916.2005.00763.x.
[21] A. Polotai, K. Breece, E. Dickey, C. Randall, A. Ragulya, A Novel Approach to Sintering Nanocrystalline Barium Titanate Ceramics, Journal of the American Ceramic Society. 88 (2005) 3008–3012. https://doi.org/10.1111/j.1551-2916.2005.00552.x.

[22] W. Meng, R. Zuo, S. Su, X. Wang, L. Li, Two-step sintering and electrical properties of sol–gel derived 0.94(Bi0.5Na0.5)TiO3–0.06BaTiO3 lead-free ceramics, Journal of Materials Science: Materials in Electronics. 22 (2011) 1841–1847. https://doi.org/10.1007/s10854-011-0371-4.
[23] J. Ding, Y. Liu, Y. Lu, H. Qian, H. Gao, H. Chen, C. Ma, Enhanced energy-storage properties of 0.89Bi 0.5 Na 0.5 TiO 3 –0.06BaTiO 3 –0.05K 0.5 Na 0.5 NbO 3 lead-free anti-ferroelectric ceramics by two-step sintering method, Materials Letters. 114 (2014) 107–110. https://doi.org/10.1016/j.matlet.2013.09.103.
[24] J. Fang, X. Wang, Z. Tian, C. Zhong, L. Li, R. Zuo, Two-Step Sintering: An Approach to Broaden the Sintering Temperature Range of Alkaline Niobate-Based Lead-Free Piezoceramics: Rapid Communications of the American Ceramic Society, Journal of the American Ceramic Society. 93 (2010) 3552–3555. https://doi.org/10.1111/j.1551-2916.2010.04085.x.
[25] J. Zhang, Y. Qin, Y. Gao, W. Yao, M. Zhao, Improvement of Physical Properties for KNN-based Ceramics by Modified Two-Step Sintering, Journal of the American Ceramic Society. 97 (2014) 759–764. https://doi.org/10.1111/jace.12794.
[26] S. Wang, Y. Chen, L. Zhang, C. Ren, F. Chen, K.S. Brinkman, Two-Step Reactive Aid Sintering of BaZr0.8Y0.2O3−δ Proton-Conducting Ceramics, Journal of Electronic Materials. 44 (2015) 4898–4906. https://doi.org/10.1007/s11664-015-4078-9.
[27] S. Nikodemski, J. Tong, R. O'Hayre, Solid-state reactive sintering mechanism for proton conducting ceramics, Solid State Ionics. 253 (2013) 201–210. https://doi.org/10.1016/j.ssi.2013.09.025.
[28] S. Ricote, N. Bonanos, H.J. Wang, B.A. Boukamp, Conductivity study of dense BaZr0.9Y0.1O(3−δ) obtained by spark plasma sintering, Solid State Ionics. 213 (2012) 36–41. https://doi.org/10.1016/j.ssi.2011.02.011.
[29] J. Guo, A.L. Baker, H. Guo, M. Lanagan, C.A. Randall, Cold sintering process: A new era for ceramic packaging and microwave device development, Journal of the American Ceramic Society. 100 (2017) 669–677. https://doi.org/10.1111/jace.14603.
[30] H. Guo, T.J.M. Bayer, J. Guo, A. Baker, C.A. Randall, Cold sintering process for 8 mol%Y 2 O 3 -stabilized ZrO 2 ceramics, Journal of the European Ceramic Society. 37 (2017) 2303–2308. https://doi.org/10.1016/j.jeurceramsoc.2017.01.011.
[31] S.S. Berbano, J. Guo, H. Guo, M.T. Lanagan, C.A. Randall, Cold sintering process of Li $_{1.5}$ Al $_{0.5}$ Ge $_{1.5}$ (PO $_4$) $_3$ solid electrolyte, Journal of the American Ceramic Society. 100 (2017) 2123–2135. https://doi.org/10.1111/jace.14727.
[32] J.-P. Maria, X. Kang, R.D. Floyd, E.C. Dickey, H. Guo, J. Guo, A. Baker, S. Funihashi, C.A. Randall, Cold sintering: Current status and prospects, Journal of Materials Research. 32 (2017) 3205–3218. https://doi.org/10.1557/jmr.2017.262.
[33] J. Guo, H. Guo, A.L. Baker, M.T. Lanagan, E.R. Kupp, G.L. Messing, C.A. Randall, Cold Sintering: A Paradigm Shift for Processing and Integration of Ceramics, Angewandte Chemie International Edition. 55 (2016) 11457–11461. https://doi.org/10.1002/anie.201605443.
[34] S. Miyoshi, Y. Akao, N. Kuwata, J. Kawamura, Y. Oyama, T. Yagi, S. Yamaguchi, Low-Temperature Protonic Conduction Based on Surface Protonics: An Example of Nanostructured Yttria-Doped Zirconia, Chem. Mater. 26 (2014) 5194–5200. https://doi.org/10.1021/cm5012923.

[35] Q. Hu, H. Zhao, S. Ouyang, Understanding water structure from Raman spectra of isotopic substitution H 2 O/D 2 O up to 573 K, Physical Chemistry Chemical Physics. 19 (2017) 21540–21547. https://doi.org/10.1039/C7CP02065A.
[36] A. M. Amado, P.J. A. Ribeiro-Claro, H/D and D/H exchange rates in α-cyclodextrin and α-cyclodextrin inclusion compounds Raman spectroscopic study, Journal of the Chemical Society, Faraday Transactions. 93 (1997) 2387–2390. https://doi.org/10.1039/A702004J.
[37] A.M. da Silva, T. Steiner, W. Saenger, J. Empis, J.J.C. Teixeira-Dias, Dynamics of H/D and D/H exchanges in β-cyclodextrindodecahydrate observed in real time: effects from zero-point vibrationalenergy, Chem. Commun. (1997) 465–466. https://doi.org/10.1039/A607721H.
[38] E. Iizuka, T. Horikawa, B. Tsuchiya, K. Soda, K. Morita, H. Iwahara, Anomalous Difference between Replacements of D–H and H–D in Oxide Ceramics by Exposure to Air Containing H2O and D2O Vapors, Jpn. J. Appl. Phys. 40 (2001) 3343. https://doi.org/10.1143/JJAP.40.3343.
[39] W. Luo, D.F. Cowgill, R.A. Causey, Thermodynamic and Kinetic Characterization of Hydrogen−Deuterium Exchange in β-Phase Palladium, J. Phys. Chem. B. 113 (2009) 12978–12987. https://doi.org/10.1021/jp903633b.
[40] W. Luo, D.F. Cowgill, Kinetics of Hydrogen Isotope Exchange in β-Phase Pd–H–D, J. Phys. Chem. C. 119 (2015) 18099–18109. https://doi.org/10.1021/acs.jpcc.5b06848.
[41] M. Shirpour, G. Gregori, R. Merkle, J. Maier, On the proton conductivity in pure and gadolinium doped nanocrystalline cerium oxide, Physical Chemistry Chemical Physics. 13 (2011) 937–940. https://doi.org/10.1039/C0CP01702G.
[42] D.B. Asay, S.H. Kim, Evolution of the Adsorbed Water Layer Structure on Silicon Oxide at Room Temperature, J. Phys. Chem. B. 109 (2005) 16760–16763. https://doi.org/10.1021/jp053042o.
[43] S. Ø. Stub, E. Vøllestad, T. Norby, Protonic surface conduction controlled by space charge of intersecting grain boundaries in porous ceramics, Journal of Materials Chemistry A. 6 (2018) 8265–8270. https://doi.org/10.1039/C7TA11088J.
[44] C.-Y. Wu, K.-J. Tu, J.-P. Deng, Y.-S. Lo, C.-H. Wu, Markedly Enhanced Surface Hydroxyl Groups of TiO2 Nanoparticles with Superior Water-Dispersibility for Photocatalysis, Materials. 10 (2017) 566. https://doi.org/10.3390/ma10050566.
[45] Y. Zhou, X. Guan, H. Zhou, K. Ramadoss, S. Adam, H. Liu, S. Lee, J. Shi, M. Tsuchiya, D.D. Fong, S. Ramanathan, Strongly correlated perovskite fuel cells, Nature. 534 (2016) 231–234. https://doi.org/10.1038/nature17653.
[46] Y. Yamazaki, R. Hernandez-Sanchez, S.M. Haile, High total proton conductivity in large-grained yttrium-doped barium zirconate, Chemistry of Materials. 21 (2009) 2755–2762. https://doi.org/10.1021/cm900208w.
[47] J.G. Lyagaeva, G.K. Vdovin, D.A. Medvedev, Distinguishing Bulk and Grain Boundary Transport of a Proton-Conducting Electrolyte by Combining Equivalent Circuit Scheme and Distribution of Relaxation Times Analyses, (2019). https://doi.org/10.1021/acs.jpcc.9b05705.
[48] J. Gao, Y. Liu, Y. Meng, M. Hu, K.S. Brinkman, Fluoride-Based Anion Doping: A New Strategy for Improving the Performance of Protonic Ceramic Conductors of the Form $BaZrO_3$, ChemElectroChem. 7 (2020) 2242–2247. https://doi.org/10.1002/celc.202000154.

[49] S. Tao, J.T.S. Irvine, Conductivity studies of dense yttrium-doped BaZrO3 sintered at 1325 °C, Journal of Solid State Chemistry. 180 (2007) 3493–3503. https://doi.org/10.1016/j.jssc.2007.09.027.
[50] K. Nomura, H. Kageyama, Transport properties of Ba(Zr0.8Y0.2)O3 - δ perovskite, Solid State Ionics. 178 (2007) 661–665. https://doi.org/10.1016/j.ssi.2007.02.010.
[51] R.B. Cervera, Y. Oyama, S. Miyoshi, K. Kobayashi, T. Yagi, S. Yamaguchi, Structural study and proton transport of bulk nanograined Y-doped BaZrO3 oxide protonics materials, Solid State Ionics. 179 (2008) 236–242. https://doi.org/10.1016/j.ssi.2008.01.082.
[52] Z. Sun, E. Fabbri, L. Bi, E. Traversa, Electrochemical Properties and Intermediate-Temperature Fuel Cell Performance of Dense Yttrium-Doped Barium Zirconate with Calcium Addition, Journal of the American Ceramic Society. 95 (2012) 627–635. https://doi.org/10.1111/j.1551-2916.2011.04795.x.
[53] W. Sun, Z. Shi, M. Liu, L. Bi, W. Liu, An Easily Sintered, Chemically Stable, Barium Zirconate-Based Proton Conductor for High-Performance Proton-Conducting Solid Oxide Fuel Cells, Advanced Functional Materials. 24 (2014) 5695–5702. https://doi.org/10.1002/adfm.201401478.
[54] K.Y. Park, Y. Seo, K.B. Kim, S.J. Song, B. Park, J.Y. Park, Enhanced proton conductivity of yttrium-doped barium zirconate with sinterability in protonic ceramic fuel cells, Journal of Alloys and Compounds. 639 (2015) 435–444. https://doi.org/10.1016/j.jallcom.2015.03.168.
[55] K. Yang, J.X. Wang, Y.J. Xue, M. Sen Wang, C.R. He, Q. Wang, H. Miao, W.G. Wang, Synthesis, sintering behavior and electrical properties of Ba(Zr 0.1Ce0.7Y0.2)O3-δ and Ba(Zr0.1Ce0.7Y0.1Yb0.1)O 3-δ proton conductors, Ceramics International. 40 (2014) 15073–15081. https://doi.org/10.1016/j.ceramint.2014.06.115.
[56] A. Lesnichyova, A. Stroeva, S. Belyakov, A. Farlenkov, N. Shevyrev, M. Plekhanov, I. Khromushin, T. Aksenova, M. Ananyev, A. Kuzmin, Water Uptake and Transport Properties of La1−xCaxScO3−α Proton-Conducting Oxides, Materials. 12 (2019) 2219. https://doi.org/10.3390/ma12142219.
[57] B. Scherrer, M.V.F. Schlupp, D. Stender, J. Martynczuk, J.G. Grolig, H. Ma, P. Kocher, T. Lippert, M. Prestat, L.J. Gauckler, On Proton Conductivity in Porous and Dense Yttria Stabilized Zirconia at Low Temperature, Advanced Functional Materials. 23 (2013) 1957–1964. https://doi.org/10.1002/adfm.201202020.
[58] R. Casasnovas, M. Adrover, J. Ortega-Castro, J. Frau, J. Donoso, F. Muñoz, C–H Activation in Pyridoxal-5′-phosphate Schiff Bases: The Role of the Imine Nitrogen. A Combined Experimental and Computational Study, J. Phys. Chem. B. 116 (2012) 10665–10675. https://doi.org/10.1021/jp303678n.
[59] D. Poetzsch, R. Merkle, J. Maier, Proton conductivity in mixed-conducting BSFZ perovskite from thermogravimetric relaxation, Phys. Chem. Chem. Phys. 16 (2014) 16446. https://doi.org/10.1039/C4CP00459K.
[60] L. Agosta, E.G. Brandt, A.P. Lyubartsev, Diffusion and reaction pathways of water near fully hydrated TiO_2 surfaces from *ab initio* molecular dynamics, The Journal of Chemical Physics. 147 (2017) 024704. https://doi.org/10.1063/1.4991381.
[61] F. Maglia, I.G. Tredici, G. Spinolo, U. Anselmi-Tamburini, Low temperature proton conduction in bulk nanometric TiO_2 prepared by high-pressure field assisted sintering, J. Mater. Res. 27 (2012) 1975–1981. https://doi.org/10.1557/jmr.2012.158.